

# Sequence Analysis Using the Bézier Curve

Taslim Murad<sup>1\*</sup>, Sarwan Ali<sup>2\*</sup> (✉), and Murray Patterson<sup>1</sup>

<sup>1</sup> Department of Computer Science, Georgia State University, Atlanta, GA, USA  
tmurad2@student.gsu.edu, mpatterson30@gsu.edu

<sup>2</sup> Department of Neurology, Columbia University, New York, NY, USA  
sa4559@columbia.edu

\* Equal Contribution

**Abstract.** The analysis of sequences (e.g., protein, DNA, and SMILES string) is essential for disease diagnosis, biomaterial engineering, genetic engineering, and drug discovery domains. Conventional analytical methods focus on transforming sequences into numerical representations for applying machine learning/deep learning-based sequence characterization. However, their efficacy is constrained by the intrinsic nature of deep learning (DL) models, which tend to exhibit suboptimal performance when applied to tabular data. An alternative group of methodologies endeavors to convert biological sequences into image forms by applying the concept of Chaos Game Representation (CGR). However, a noteworthy drawback of these methods lies in their tendency to map individual elements of the sequence onto a relatively small subset of designated pixels within the generated image. The resulting sparse image representation may not adequately encapsulate the comprehensive sequence information, potentially resulting in suboptimal predictions. In this study, we introduce a novel approach to transform sequences into images using the Bézier curve concept for element mapping. Mapping the elements onto a curve enhances the sequence information representation in the respective images, hence yielding better DL-based classification performance. We employed different sequence datasets to validate our system by using different classification tasks, and the results illustrate that our Bézier curve method is able to achieve good performance for all the tasks.

**Keywords:** Sequence Classification, Image Analysis, Classification, Chaos Game Representation.

## 1 Introduction

Sequence analysis, especially protein sequence analysis [35,12], serves as a foundational undertaking within the field of bioinformatics, possessing a broad spectrum of applications encompassing drug exploration, ailment detection, and tailored medical interventions. The comprehension of attributes, functionalities, configurations, and evolutionary patterns inherent to biological sequences holds paramount significance for elucidating biological mechanisms and formulating effective therapeutic approaches [29].

Traditional phylogenetic approaches [8,23] for the analysis of biological sequences are no longer effective due to the availability of large sequence data, as these methods

are not scalable due to being computationally very expensive. They also require extensive domain knowledge, and incomplete knowledge easily hinders the results. Numerous feature-engineering-based works exist to encode sequences into numerical form to perform machine learning (ML)/Deep learning (DL)-based analysis, as ML/DL models are well-known to tackle large datasets efficiently. For example, OHE [17] builds binary vectors against the sequences. However, it is alignment-based, and sequence alignment is an expensive process. The generated vectors by OHE are also very sparse and highly dimensional. Another set of approaches [1,21] follows the  $k$ -mers concept to obtain feature embeddings. But they also undergo sparsity challenges and are usually computationally expensive. Moreover, some approaches [31,36] utilize a neural network to extract feature embeddings from the sequences to perform analysis. However, they usually require large training data to achieve optimal performance, and acquiring more data is usually an expensive procedure for medical data.

An alternative approach for biological sequence analysis entails the transformation of sequences into image representations. This adaptation facilitates the utilization of sophisticated DL vision models to address sequence analysis objectives, as DL models are very popular in achieving state-of-the-art performance for image classification. FCGR [20], RandomCGR [25], and protein secondary structure prediction [38] are some of the methods that fall under this category. They are based on the concept of CGR(Chaos Game Representation) [16]. Such mappings are between amino acids and specific pixels of the generated images, which can result in suboptimal representation due to capturing the information in a sparse way about amino acids/nucleotides of a sequence in its respective constructed image.

Therefore, in this work, we propose a method based on the Bézier curve [9] to translate biological sequences into images to enable the application of DL models on them. Bézier curve [9] is a smooth and continuous parametric curve that is defined by a set of discrete control points. It is widely used to draw shapes, especially in computer graphics and animation. It has been used in the representation learning domain previously but mainly focusing on extracting numerical features, such as in [13] which does  $n$ -step sequence prediction based on the Bézier curve, [19] proposed end-to-end text spotting using the Bézier curve, [28] does map construction, etc. However, we aim to utilize the Bézier curve to formulate an efficient mechanism for transforming biological sequences into images by effectively mapping the components of a sequence onto a curve. Each component, or character (an amino acid, nucleotide, etc.) of a sequence is represented by multiple lines on the curve which enable more information to be captured in the respective image, hence producing a better representation. The goal of using Bezier curves is to create a visualization that aids in the analysis of protein sequences. This visualization can allow researchers to explore patterns and trends that might provide insights into protein structure and function.

Our contributions in this work are as follows,

1. We present a novel approach for converting biological sequences into images utilizing the Bézier function. By harnessing the capabilities of the Bézier curve in conjunction with deep learning analytical models, we can foster a more profound comprehension of these sequences. This innovative technique holds promise for

advancing our understanding of biological data and enabling more robust analysis and insights.

- Using three distinct protein datasets (protein subcellular dataset, Coronavirus host dataset, ACP dataset) for validating our proposed technique, we show that our method is able to achieve high performance in terms of predictive performance for various classification tasks.

The rest of the paper is organized as follows: Section 2 talks about the literature review, Section 3 discusses the proposed approach in detail, Section 4 highlights the experimental setup details of our work, Section 5 discusses the results obtained, and Section 6 concludes the paper.

## 2 Literature Review

Biological sequence analysis is an active research area in the domain of bioinformatics. Numerous works exist to tackle biological sequences, and most of them aim to map sequences into machine-readable form to perform further ML/DL-based analysis on them. For instance, OHE [17] constructs binary vectors to represent the sequences, but these vectors are very sparse and suffer from the curse of dimensionality challenge. Likewise, Spike2Vec [1] & PWkmer [21] design feature embeddings based on the  $k$ -mers of the sequences. However, they also undergo the sparsity issue, and computation of  $k$ -mers is usually an expensive process, especially for long sequences. Moreover, some approaches [31,36] employ a neural network to obtain the numerical embeddings of the sequences, but their large training data requirement to attain optimal performance is an expensive requirement. Furthermore, a set of works (Protein Bert [4], Seqvec [11], UDSMProt [33]) follows the utilization of pre-trained models for extracting features from the protein sequences to assist the classification tasks. However, these mechanisms are computationally very costly. Several kernel matrix-based works [5,2] are put forward to deal with protein sequence classification. These methods build a symmetric kernel matrix to represent the sequences by capturing the similarity between them, and this matrix is further utilized as input to the classification tasks. But the kernel matrix is usually of high dimensions, and loading it is memory inefficient. An alternative set of techniques transforms the sequences into images, particularly for enabling the application of sophisticated DL analytical models in the domain of bio-sequence analysis. These methodologies [24,38,25,20] are usually built upon the concept of CGR [16]. They follow an iterative mechanism to construct the images. However, these methods map the components (amino acids/nucleotides) of a sequence to specific pixels in the corresponding generated image, while our method maps them onto a Bézier curve, resulting in more intuitive and easy-to-interpret visualization.

## 3 Proposed Approach

This section discusses the details of our proposed method, which converts protein sequences into images following the concept of the Bézier curve to enable the application of sophisticated DL models on the sequence classification tasks. The general formula [3] of the Bézier curve is

$$BZ(t) = \sum_{i=0}^n \binom{n}{i} t^i (1-t)^{n-i} P_i \quad (1)$$

where  $0 \leq t \leq 1$ ,  $P_i$  are known as control points and are elements of  $\mathbb{R}^k$ , and  $k \leq n$ .

To construct the protein images, we employ a Bézier curve with  $n = 3$  and  $k = 2$ . As images consist of x and y coordinates, therefore  $k = 2$  is used. The formulas to determine the coordinates for representing an amino acid in the respective generated image are,

$$x = (1-t)^3 \cdot P_{0_x} + 3 \cdot (1-t)^2 \cdot t \cdot P_{1_x} + 3 \cdot (1-t) \cdot t^2 \cdot P_{2_x} + t^3 \cdot P_{3_x} \quad (2)$$

$$y = (1-t)^3 \cdot P_{0_y} + 3 \cdot (1-t)^2 \cdot t \cdot P_{1_y} + 3 \cdot (1-t) \cdot t^2 \cdot P_{2_y} + t^3 \cdot P_{3_y} \quad (3)$$

where,  $(P_{0_x}, P_{0_y})$ ,  $(P_{1_x}, P_{1_y})$ ,  $(P_{2_x}, P_{2_y})$ , &  $(P_{3_x}, P_{3_y})$  denote the x & y coordinates of the four distinct control points respectively.

The algorithm and workflow of creating Bézier-based images are illustrated in Algorithm 1 and Figure 1, respectively. We can observe that given a sequence and number of parameters  $m$  as input, the algorithm and workflow yield an image as output. Note that  $m$  indicates the parameter  $t$  shown in the above equations. The process starts by computing the control points by considering the unique amino acids of the given sequence and their respective ASCII values (numerical), as depicted in steps 4-6 of the algorithm and step (b) of the workflow. A control point is made of a pair of numerical values representing the x and y coordinates, where x is assigned the index of the first occurrence of the respective unique amino acid and y holds its ASCII value. Moreover,  $m$  linearly spaced random pairs belonging to  $[0,1]$  are generated as parameters (mentioned in step 9 and step (c) of the algorithm and workflow respectively). Note that we used  $m = 200$  for our experiments. Then the deviation pair points are generated for every amino acid of the sequence (as exhibited in step 15 of the algorithm and step (d) of the workflow). We utilized 3 deviation pairs to conduct our experiments. After that, modified pair points are obtained by adding the deviation pairs to the corresponding amino acid's control point pair respectively, as shown in step 16 of the algorithm and step (e) of the workflow. Then the Bézier pair points are extracted from the Bézier function by employing (2) and (3) (as presented in step 19 and step (f) of the algorithm and workflow respectively). Finally, the Bézier pairs are used as x and y coordinates to plot the image (as shown in step 23 and step (g) of the algorithm and workflow respectively). Note that, we get multiple Bézier pairs depending on the value of  $m$  and we plot all the pairs in the created image to represent the respective amino acid in the image.

As Bézier curves are known for their ability to smoothly interpolate control points, using them to connect control points for representing amino acids ensures a visually smooth transition between points, making the visualization more intuitive and easy to interpret. Moreover, introducing randomness to the control points by adding deviations results in controlled CGR. While the approach deviates from traditional CGR, it helps reveal patterns that might not be apparent in regular CGR due to the scattering of control points. This randomness mimics the inherent variability and noise present in biological

**Algorithm 1** Bézier Curve Based Image Generation

---

**Input:** Sequence *seq*, No. of Parameters *m*  
**Output:** Image *img*

```

1: conPoint = {}                                ▷ dictionary for control points
2: for i, aa ∈ seq do:                          ▷ every unique amino acid aa in seq
3:   conPoint[aa] = [i, ASCII(aa)]           ▷ assign control point the index i and ASCII of aa
4: end for
5: xCord = []                                   ▷ list for x coordinates
6: yCord = []                                   ▷ list for y coordinates
7: t_Val = Get m pairs ∈ [0, 1]                ▷ list of m pairs of parameters
8: ite = 3                                       ▷ no. of deviations pair points. It can have any value.
9: for a ∈ seq : do                               ▷ every amino acid a in seq
10:  org_point = conPoint[a]                    ▷ control point of a
11:  points = [org_point]
12:  for i ∈ (ite) : do
13:    dev = Get_Random_Pair                       ▷ get a random pair
14:    mod_point = org_point + dev                 ▷ get a modified control point
15:    points.append(mod_point)
16:  end for
17:  curve_point = Get_Bezier_Point(points, t_Val) ▷
    get bezier curve points from bezier func
18:  xCord = curve_point[:0]                      ▷ get x coords of curve
19:  yCord = curve_point[:1]                      ▷ get y coords of curve
20: end for
21: img = plot(xCord, yCord)                   ▷ get image by plotting x & y coords
22: return(img)

```

---

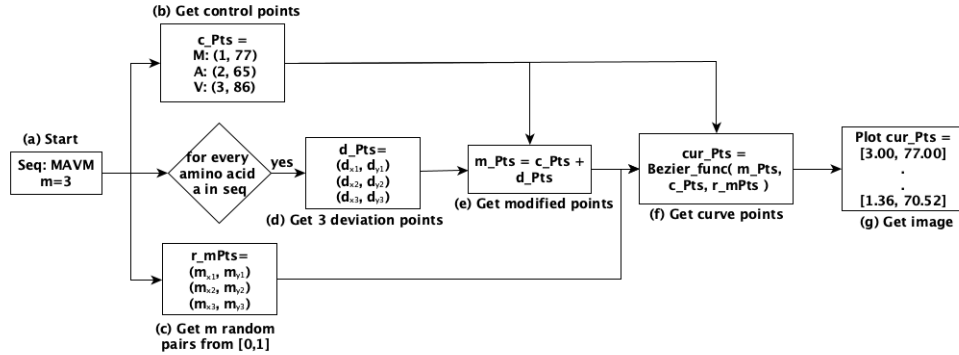


Fig. 1: The workflow of our system to create an image from a given sequence and a number of parameters *m*. We have used "MAVM" as an input sequence here. Note that the *cur\_Pts* consists of a set of values for x coordinates and y coordinates.

sequences. It can be justified as an attempt to capture the inherent variability in pro-

Dataset	Description
Protein Subcellular Localization	It has 5959 unaligned protein sequences distributed among 11 unique subcellular locations. The associated subcellular location is predicted for a given protein sequence as input.
Coronavirus Host	The unaligned spike protein sequences from various clades of the Coronaviridae family are collected to form this dataset. It contains 5558 spike sequences distributed among 22 unique hosts.
Anticancer Peptides (ACPs)	It consists of 949 unaligned peptide-protein sequences along with their respective anticancer activity on the breast cancer cell lines distributed among the 4 unique target labels.
Human DNA [14]	It consists of 2,000 unaligned Human DNA nucleotide sequences which are distributed among seven unique gene families. These gene families are used as labels for classification. The gene families are G Protein Coupled, Tyrosine Kinase, Tyrosine Phosphatase, Synthetase, Synthase, Ion Channel, and Transcription Factor containing 215, 299, 127, 347, 319, 94, & 599 instances respectively.
SMILES String [30]	It has 6,568 SMILES strings distributed among ten unique drug subtypes extracted from the DrugBank dataset. We employ the drug subtypes as a label for doing classification. The drug subtypes are Barbiturate [EPC], Amide Local Anesthetic [EPC], Non-Standardized Plant Allergenic Extract [EPC], Sulfonylurea [EPC], Corticosteroid [EPC], Nonsteroidal Anti-inflammatory Drug [EPC], Nucleoside Metabolic Inhibitor [EPC], Nitroimidazole Antimicrobial [EPC], Muscle Relaxant [EPC], and Others with 54, 53, 30, 17, 16, 15, 11, 10, 10, & 6352 instances respectively.
Music Genre [18]	This data has 1,000 audio sequences belonging to 10 unique music genres, where each genre contains 100 sequences. We perform music genre classification tasks using this dataset. The genres are Blues, Classical, Country, Disco, Hiphop, Jazz, Metal, Pop, Reggae, and Rock.

Table 1: The summary of all the datasets used for evaluation.

tein sequences that can arise due to mutations, structural differences, or experimental variations.

## 4 Experimental Evaluation

This section discusses the details of the experimental setup used to perform the experiments. It highlights the datasets, baseline methods, and classification models. All experiments are carried out on a server having Intel(R) Xeon(R) CPU E7-4850 v4 @ 2.40GHz with Ubuntu 64-bit OS (16.04.7 LTS Xenial Xerus) having 3023 GB memory. We employed Python for implementation.

### 4.1 Data Statistics

We have used 3 distinct protein sequence datasets, a nucleotide-based dataset, a musical dataset, and a SMILES string dataset to evaluate our proposed system. The reason to use such diversified datasets is to show the generalizability of our method for any type of sequence. Each dataset is summarized in Table 1. Further details of the datasets are given in Appendix C.

### 4.2 Baseline Models

We compared the performance of our proposed method with various baselines. These baselines are categorized into three groups: feature-engineering-based baselines, kernel-

Category	Method	Description
Feature Engineering based methods	OHE	It generates binary vector-based numerical embeddings of the sequences.
	WDGRL	It is an unsupervised approach that uses a neural network to extract numerical features from the sequences.
Kernel Method	String Kernel	Given a set of sequences as input, this method designs $n \times n$ kernel matrix that can be used with kernel classifiers or with kernel PCA to get feature vectors
Image based methods	FCGR	It maps the protein sequences into images by following the concept of CGR and constructs n-flakes-based images.
	RandomCGR	This method follows a random function for determining the coordinates of amino acids of protein sequences to create images.
	Spike2CGR	This technique combines CGR with minimizers and $k$ -mers concepts to determine the images of given protein sequences.

Table 2: The summary of the baseline methods used for evaluation.

based baseline, and image-based baselines. The feature-engineering-based baselines (OHE [17]), WDGRL [31]) consist of methods that map the bio-sequences into numerical vectors to enable the application of ML/DL models on them. In the kernel-based baseline (String kernel [2,5]), the goal is to design a kernel matrix and then use kernel PCA to get the final embeddings, which can then be used as input to classical ML models, like SVM, Naive Bayes (NB), Multi-Layer Perceptron (MLP), K-Nearest Neighbors (KNN), Random Forest (RF), Logistic Regression (LR), and Decision Tree (DT), to perform sequence classification. The image-based baselines (FCGR [20], Random-CGR [25], Spike2CGR [24]) aim to transform the bio-sequences into images to perform DL-based classification. The baseline methods used are summarized in Table 2 (further details are in Appendix D).

### 4.3 Classification Models

In the realm of classification tasks, we have employed two distinct categories of classifiers: Image models and Tabular models. For both categories, the data follows 80 – 20% split for train-test sets, and the train set is further divided into 70 – 30% train-validation sets. These splits follow a stratified sampling strategy to keep the distribution the same as given in the original data.

**Image Models:** These models are used for image-based classification. We construct four custom convolutional neural networks (CNNs) classifiers with varying numbers of hidden layers to do the classification tasks. These models are referred to as 1-layer, 2-layer, 3-layer & 4-layer CNN classifiers, and they consist of 1, 2, 3, & 4 hidden block A modules respectively. A block A module contains a convolution layer followed by a ReLU activation function and a max-pool layer. These custom CNN networks are employed to investigate the impact of increasing the number of hidden layers on the final predictive performance. Moreover, a vision transformer model (ViT) is also used by us for performing the classification tasks. As ViT is known to utilize the power of transformer architecture, we want to see its impact on our bio-sequence datasets classifications. Furthermore, we also examine the consequences of using pre-trained vision models for classifying our datasets, and for that, we used pre-trained ResNet-50 [10],

Category	Model	Description
Custom CNN	1-layer CNN	A custom CNN model with one hidden block A module (layer).
	2-layer CNN	A custom CNN model with two hidden block A modules (layers).
	3-layer CNN	A custom CNN model with three hidden block A modules (layers).
	4-layer CNN	A custom CNN model with four hidden block A modules (layers).
Transformer	ViT	A vision transformer classifier following the architecture of the transformer to do image-based classification.
	VGG19	The pre-trained VGG19 [32] is employed to do image-based classification.
Pre-trained	ResNet-50	The pre-trained ResNet-50 [10] is employed to do image-based classification.
	EfficientNet	The pre-trained EfficientNet [34] is employed to do image-based classification.
	DenseNet	The pre-trained DenseNet [15] is employed to do image-based classification.

Table 3: The summary of all the image models used for evaluation.

EfficientNet [34], DenseNet [15] and VGG19 [32] models. The image classifiers are summarized in Table 3, and further details about their respective architectures and hyperparameters can be viewed in Appendix E.1.

**Tabular Models:** These models aim to classify the numerical data. We have used two distinct DL tabular models in our experimentation, which are known as the 3-layer tab CNN model & the 4-layer tab CNN model. 3-layer tab CNN model consists of 3 hidden linear layers, while 4-layer tab CNN has 4 hidden linear layers. In each of the classifiers, the hidden layers are followed by a classification linear layer. The hyperparameters chosen by us after fine-tuning are 0.001 learning rate, ADAM optimizer, NLL loss function, and 10 training epochs. Moreover, the input vectors from WDGRL are of dimensions 10, as it transforms the data into low dimensional space. Furthermore, we employed some ML models (SVM, Naive Bayes (NB), Multi-Layer Perceptron (MLP), K-Nearest Neighbors (KNN), Random Forest (RF), Logistic Regression (LR), and Decision Tree (DT)) to classify the kernel-method-based feature embeddings.

## 5 Results and Discussion

This section provides an extensive discussion of the classification results obtained by our proposed method and the baseline approaches for different classification tasks.

### 5.1 Protein Subcellular Dataset’s Performance

The classification results of the protein subcellular dataset via different evaluation metrics are mentioned in Table 4. We can observe that in the case of the custom CNN models, the performance stopped increasing after two layers. It could be because of the dataset being small in size which causes the gradient vanishing problem. Moreover, for the ViT model although the Bézier images have maximum performance as compared to the FCGR and RandomCGR images, however, the overall performance gained by the ViT model is less than the custom CNN models. A reason for this could be the dataset being small in size as ViT typically requires substantial training data to surpass CNN models. Additionally, in ViT a global attention mechanism is used which focuses on

the entire image, but in the images generated by all three methods (FCGR, Random-CGR & Bézier) the pertinent information is concentrated in specific pixels, with the remaining areas being empty. Consequently, the global attention mechanism may not be as efficient for these images as a local operation-based CNN model, which is tailored to capture localized features efficiently. The feature-engineering-based methods are yielding very low performance as compared to our image-based methods (especially FCGR & Bézier) indicating that the image-based representation of bio-sequences is more effective in terms of classification performance over the tabular one. The pre-trained ResNet-50 classifier corresponding to the Bézier method has the optimal predictive performance for all the evaluation metrics. It shows that the ResNet-50 is able to generalize well to the Bézier generated images. It may be due to the architecture of ResNet (like skip connections) enabling the learning on our small dataset. Overall, the pre-trained models (ResNet, VGG19, & EfficientNet) are performing well for the Bézier based images, except the DenseNet model. A reason for DenseNet having very bad performance could be the dataset being small, as DenseNet typically requires large data to yield good performance. Furthermore, among the image-based methods, our Bézier method is tremendously outperforming the baselines for every evaluation metric corresponding to all the vision DL classifiers. This can be because the average length of sequences in the protein subcellular localization dataset is large and our technique uses the Bézier curve to map each amino acid, so a large number of amino acids results in more effective capturing of information about the sequences in their respective constructed images.

We have also added results of the Spike2CGR baseline method in Table 4 and we can observe that this method is underperforming for all the classifiers for every evaluation metric as compared to our proposed Bézier method. This indicates that the images created by the Bézier technique are of high quality in terms of classification performance as compared to the Spike2CGR-based images. Moreover, the String kernel-based results also showcase very low performance as compared to the image-based method, hence again indicating that converting sequences to images gives a more effective representation than mapping them to vectors.

## 5.2 Coronavirus Host Dataset's Performance

The Coronavirus host dataset-based classification performance via various evaluation metrics is reported in Appendix F.1 Table 14. We can observe that for the custom CNN models, the performance is not directly proportional to the number of hidden layers, i.e., increasing the number of hidden layers does not result in better performance, as most of the top values reside corresponding to the 1-layer CNN model and the 2-layer CNN model. This could be because the host dataset is not large enough to tackle a heavy CNN model, hence ending up having a gradient vanishing problem, which stops the model from learning. Apart from that, the ViT model is exhibiting lower performance than the custom CNN model and it can be yet again due to the dataset being small. Moreover, among the pre-trained models, ResNet-50 & VGG19 are showcasing nearly similar performance as the custom CNN classifiers (with Bézier-based images yielding maximum performance), which indicates that these models are able to generalize well using the images created by our Bézier method. However, DenseNet and

Category	DL Model	Method	Acc. ↑	Prec. ↑	Recall ↑	F1 (Weig.) ↑	F1 (Macro) ↑	ROC AUC ↑	Train Time (hrs.) ↓	
Tabular Models	3-Layer Tab-CNN	OHE	0.449	0.405	0.449	0.401	0.227	0.667	0.398	
		WDGRL	0.458	0.315	0.458	0.354	0.163	0.751	0.109	
	4-Layer Tab-CNN	OHE	0.404	0.409	0.404	0.384	0.215	0.657	0.525	
		WDGRL	0.457	0.309	0.457	0.351	0.161	0.708	0.130	
String Kernel	-	SVM	0.496	0.510	0.496	0.501	0.395	0.674	5.277	
	-	NB	0.301	0.322	0.301	0.265	0.243	0.593	0.136	
	-	MLP	0.389	0.390	0.389	0.388	0.246	0.591	7.263	
	-	KNN	0.372	0.475	0.372	0.370	0.272	0.586	0.395	
	-	RF	0.473	0.497	0.473	0.411	0.218	0.585	7.170	
	-	LR	0.528	0.525	0.528	0.525	0.415	0.678	8.194	
-	DT	0.328	0.335	0.328	0.331	0.207	0.568	2.250		
1-Layer Custom CNN Models	FCGR	FCGR	0.545	0.542	0.545	0.527	0.386	0.653	3.065	
		RandmCGR	0.292	0.172	0.292	0.211	0.102	0.528	6.443	
		Spike2CGR	0.460	0.453	0.460	0.432	0.277	0.603	6.879	
		Bézier	<u>0.948</u>	<u>0.919</u>	<u>0.948</u>	<u>0.931</u>	<u>0.769</u>	<u>0.890</u>	3.455	
	% impro. of Bézier from	40.3	37.7	40.3	40.4	38.3	23.7	-12.72		
	FCGR	FCGR	48.8	46.6	48.8	49.9	49.2	28.7	49.7	
	% impro. of Bézier from	48.8	46.6	48.8	49.9	49.2	28.7	49.7		
	Spike2CGR	FCGR	0.565	0.565	0.565	0.554	0.432	0.677	4.074	
	2-Layer Custom CNN Models	FCGR	FCGR	0.295	0.171	0.295	0.216	0.104	0.530	6.433
			RandmCGR	0.461	0.454	0.461	0.433	0.278	0.604	8.932
Spike2CGR			0.959	<u>0.971</u>	<u>0.959</u>	<u>0.963</u>	<u>0.904</u>	<u>0.965</u>	13.089	
Bézier			<u>0.959</u>	<u>0.971</u>	<u>0.959</u>	<u>0.963</u>	<u>0.904</u>	<u>0.965</u>	13.089	
% improv. of Bézier from	39.4	40.6	39.4	40.9	47.2	28.8	-221.28			
FCGR	FCGR	49.8	51.7	49.8	53	62.6	36.1	-2922.8		
% impro. of Bézier from	49.8	51.7	49.8	53	62.6	36.1	-2922.8			
Spike2CGR	FCGR	0.504	0.518	0.504	0.501	0.376	0.656	4.821		
3-Layer Custom CNN Models	FCGR	FCGR	0.303	0.186	0.303	0.228	0.110	0.532	8.930	
		RandmCGR	0.429	0.430	0.429	0.421	0.287	0.612	3.998	
		Spike2CGR	<u>0.951</u>	<u>0.965</u>	<u>0.951</u>	<u>0.952</u>	<u>0.881</u>	<u>0.957</u>	14.983	
		Bézier	<u>0.951</u>	<u>0.965</u>	<u>0.951</u>	<u>0.952</u>	<u>0.881</u>	<u>0.957</u>	14.983	
% improv. of Bézier from	44.7	44.7	44.7	44.8	50.5	30.1	-210.78			
FCGR	FCGR	52.2	53.5	52.2	53.1	59.4	35.5	-274.7		
% impro. of Bézier from	52.2	53.5	52.2	53.1	59.4	35.5	-274.7			
Spike2CGR	FCGR	0.539	0.524	0.539	0.525	0.393	0.663	5.146		
4-Layer Custom CNN Models	FCGR	FCGR	0.311	0.181	0.311	0.229	0.110	0.536	10.234	
		RandmCGR	0.420	0.420	0.420	0.424	0.280	0.600	9.121	
		Spike2CGR	<u>0.938</u>	<u>0.958</u>	<u>0.938</u>	<u>0.944</u>	<u>0.884</u>	<u>0.959</u>	15.456	
		Bézier	<u>0.938</u>	<u>0.958</u>	<u>0.938</u>	<u>0.944</u>	<u>0.884</u>	<u>0.959</u>	15.456	
% improv. of Bézier from	39.9	43.4	39.9	41.9	49.1	29.6	-200.36			
FCGR	FCGR	51.8	53.8	51.8	52	60.4	35.9	-69.4		
% impro. of Bézier from	51.8	53.8	51.8	52	60.4	35.9	-69.4			
Spike2CGR	FCGR	0.226	0.051	0.226	0.083	0.033	0.500	0.180		
Vision Transformer	ViT	FCGR	0.222	0.049	0.222	0.080	0.033	0.500	0.154	
		RandmCGR	0.222	0.051	0.222	0.083	0.147	0.500	0.176	
		Spike2CGR	0.462	0.254	0.462	0.327	0.147	0.572	0.160	
		Bézier	0.462	0.254	0.462	0.327	0.147	0.572	0.160	
% improv. of Bézier from	23.6	20.3	23.6	24.4	11.4	7.2	11.11			
FCGR	FCGR	24	20.3	24	24.4	0	7.2	-9.09		
% impro. of Bézier from	24	20.3	24	24.4	0	7.2	-9.09			
Spike2CGR	FCGR	0.368	0.268	0.368	0.310	0.155	0.556	3.831		
ResNet-50	ResNet-50	FCGR	0.293	0.174	0.293	0.211	0.102	0.527	13.620	
		RandmCGR	0.368	0.175	0.368	0.214	0.105	0.565	10.992	
		Spike2CGR	0.964	0.967	0.964	0.961	0.907	0.948	11.415	
		Bézier	0.964	0.967	0.964	0.961	0.907	0.948	11.415	
% improv. of Bézier from	59.6	69.9	59.6	65.1	75.2	39.2	-197.96			
FCGR	FCGR	59.6	79.2	59.6	74.7	80.2	38.3	-3.8		
% impro. of Bézier from	59.6	79.2	59.6	74.7	80.2	38.3	-3.8			
Spike2CGR	FCGR	0.316	0.209	0.316	0.241	0.114	0.533	14.058		
Pretrained Vision Models	VGG-19	FCGR	0.288	0.192	0.288	0.218	0.105	0.525	26.136	
		RandmCGR	0.351	0.352	0.351	0.333	0.211	0.550	19.980	
		Spike2CGR	0.896	0.879	0.896	0.873	0.680	0.840	18.837	
		Bézier	0.896	0.879	0.896	0.873	0.680	0.840	18.837	
% improv. of Bézier from	58	67	58	63.2	56.6	30.7	-33.99			
FCGR	FCGR	54.5	52.7	54.5	56.3	46.9	29	5.7		
% impro. of Bézier from	54.5	52.7	54.5	56.3	46.9	29	5.7			
Spike2CGR	FCGR	0.081	0.006	0.081	0.012	0.013	0.500	2.001		
DenseNet	DenseNet	FCGR	0.094	0.008	0.094	0.016	0.015	0.500	1.974	
		RandmCGR	0.099	0.010	0.099	0.020	0.002	0.500	2.111	
		Spike2CGR	0.011	0.000	0.011	0.000	0.002	0.500	2.668	
		Bézier	0.011	0.000	0.011	0.000	0.002	0.500	2.668	
% improv. of Bézier from	-7	-0.6	-7	-1.2	-1.1	0	-33.33			
FCGR	FCGR	-8.8	-1	-8.8	-2	0	0	-26.3		
% impro. of Bézier from	-8.8	-1	-8.8	-2	0	0	-26.3			
Spike2CGR	FCGR	0.100	0.088	0.100	0.094	0.035	0.532	31.194		
EfficientNet	EfficientNet	FCGR	0.284	0.107	0.284	0.152	0.078	0.500	30.223	
		RandmCGR	0.320	0.230	0.320	0.230	0.200	0.500	25.497	
		Spike2CGR	0.834	0.787	0.834	0.797	0.483	0.751	20.312	
		Bézier	0.834	0.787	0.834	0.797	0.483	0.751	20.312	
% improv. of Bézier from	73.4	69.9	73.4	70.3	44.8	21.9	34.88			
FCGR	FCGR	51.4	55.7	51.4	56.7	28.3	25.1	20.3		
% impro. of Bézier from	51.4	55.7	51.4	56.7	28.3	25.1	20.3			
Spike2CGR	FCGR	0.100	0.088	0.100	0.094	0.035	0.532	31.194		
EfficientNet	EfficientNet	FCGR	0.284	0.107	0.284	0.152	0.078	0.500	30.223	
		RandmCGR	0.320	0.230	0.320	0.230	0.200	0.500	25.497	
		Spike2CGR	0.834	0.787	0.834	0.797	0.483	0.751	20.312	
		Bézier	0.834	0.787	0.834	0.797	0.483	0.751	20.312	
% improv. of Bézier from	73.4	69.9	73.4	70.3	44.8	21.9	34.88			
FCGR	FCGR	51.4	55.7	51.4	56.7	28.3	25.1	20.3		
% impro. of Bézier from	51.4	55.7	51.4	56.7	28.3	25.1	20.3			
Spike2CGR	FCGR	0.100	0.088	0.100	0.094	0.035	0.532	31.194		
EfficientNet	EfficientNet	FCGR	0.284	0.107	0.284	0.152	0.078	0.500	30.223	
		RandmCGR	0.320	0.230	0.320	0.230	0.200	0.500	25.497	
		Spike2CGR	0.834	0.787	0.834	0.797	0.483	0.751	20.312	
		Bézier	0.834	0.787	0.834	0.797	0.483	0.751	20.312	
% improv. of Bézier from	73.4	69.9	73.4	70.3	44.8	21.9	34.88			
FCGR	FCGR	51.4	55.7	51.4	56.7	28.3	25.1	20.3		
% impro. of Bézier from	51.4	55.7	51.4	56.7	28.3	25.1	20.3			
Spike2CGR	FCGR	0.100	0.088	0.100	0.094	0.035	0.532	31.194		
EfficientNet	EfficientNet	FCGR	0.284	0.107	0.284	0.152	0.078	0.500	30.223	
		RandmCGR	0.320	0.230	0.320	0.230	0.200	0.500	25.497	
		Spike2CGR	0.834	0.787	0.834	0.797	0.483	0.751	20.312	
		Bézier	0.834	0.787	0.834	0.797	0.483	0.751	20.312	
% improv. of Bézier from	73.4	69.9	73.4	70.3	44.8	21.9	34.88			
FCGR	FCGR	51.4	55.7	51.4	56.7	28.3	25.1	20.3		
% impro. of Bézier from	51.4	55.7	51.4	56.7	28.3	25.1	20.3			
Spike2CGR	FCGR	0.100	0.088	0.100	0.094	0.035	0.532	31.194		
EfficientNet	EfficientNet	FCGR	0.284	0.107	0.284	0.152	0.078	0.500	30.223	
		RandmCGR	0.320	0.230	0.320	0.230	0.200	0.500	25.497	
		Spike2CGR	0.834	0.787	0.834	0.797	0.483	0.751	20.312	
		Bézier	0.834	0.787	0.834	0.797	0.483	0.751	20.312	
% improv. of Bézier from	73.4	69.9	73.4	70.3	44.8	21.9	34.88			
FCGR	FCGR	51.4	55.7	51.4	56.7	28.3	25.1	20.3		
% impro. of Bézier from	51.4	55.7	51.4	56.7	28.3	25.1	20.3			
Spike2CGR	FCGR	0.100	0.088	0.100	0.094	0.035	0.532	31.194		
EfficientNet	EfficientNet	FCGR	0.284	0.107	0.284	0.152	0.078	0.500	30.223	
		RandmCGR	0.320	0.230	0.320	0.230	0.200	0.500	25.497	
		Spike2CGR	0.834	0.787	0.834	0.797	0.483	0.751	20.312	
		Bézier	0.834	0.787	0.834	0.797	0.483	0.751	20.312	
% improv. of Bézier from	73.4	69.9	73.4	70.3	44.8	21.9	34.88			
FCGR	FCGR	51.4	55.7	51.4	56.7	28.3	25.1	20.3		
% impro. of Bézier from	51.4	55.7	51.4	56.7	28.3	25.1	20.3			
Spike2CGR	FCGR	0.100	0.088	0.100	0.094	0.035	0.532	31.194		
EfficientNet	EfficientNet	FCGR	0.284	0.107	0.284	0.152	0.078	0.500	30.223	
		RandmCGR	0.320	0.230	0.320					

EfficientNet are demonstrating very low performance for all evaluation metrics, which may be because the size of host data is small, and these models typically need large data to attain good performance. Additionally, the feature-engineering-based methods lean towards a lower performance bound for all the evaluation metrics corresponding to both 3-layer Tab CNN & 4-layer Tab CNN, and most of the ML classifiers based on the String kernel also showcase less performance. This indicates that converting the host sequences into images can preserve more relevant information about the sequence in terms of classification performance in the respective images than converting them into vectors. Furthermore, among the image generation methods, RandomCGR has the lowest performance for every metric while Bézier (our method), Spike2CGR, and FCGR have comparable performance as they yield most of the top values for all the metrics. Overall, Bézier seems to perform well for the host classification task, implying that the images generated by it are of good quality for classification.

### 5.3 ACP Dataset's Performance

The classification performance achieved using the ACP dataset for various evaluation metrics is summarized in Appendix F.2 Table 15. We can observe that increasing the number of inner layers for the custom CNN models does not enhance the predictive performance, as 1-layer CNN & 2-layer CNN models portray higher performance. This could be because the ACP dataset is very small, so using a large model can cause a gradient vanishing challenge and, hence, hinder the learning process. Additionally, the ViT model is yielding lower performance than the custom CNN models, and it can be due to yet again the dataset being very small. Moreover, the pre-trained ResNet-50 and VGG19 models depict performance that is very similar to that of the custom CNN models. This shows that the ResNet and VGG19 models are able to generalize well to our Bézier-based data. However, the EfficientNet and DenseNet classifiers portray very low performance for every evaluation metric. It can be due to their architectures, which require large amounts of data for fine-tuning the model. However, our dataset is extremely small. Furthermore, the feature-engineering-based embedding approaches are showcasing bad performance overall (except for 4 tab CNN OHE) as compared to the image-based methods. It implies that the bio-sequences's information is effectively preserved in the respective image form rather than the vector form generated from the feature-engineering methods in terms of predictive performance. Note that, although the String kernel embedding-based ML classifiers yield the highest performances corresponding to every evaluation metric, our method's performance is also close to it, which means that our method also yields an effective representation for sequences. For the image-based embedding methods, we can notice that our method (Bézier) and the FCGR baselines illustrate comparable predictive results, while RandomCGR and Spike2CGR lean toward the lower performance bound. Overall, we can claim that the Bézier method exhibits good performance for the ACP classification task.

### 5.4 Human DNA Dataset Performance

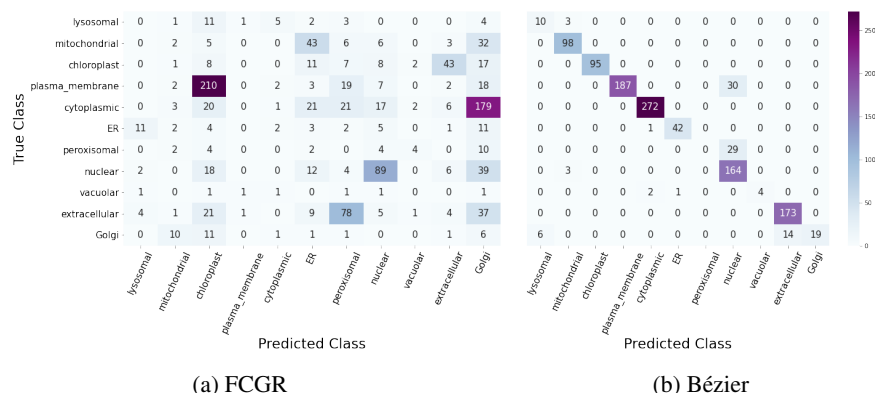


Fig. 2: Confusion matrices of **Protein Subcellular Localization dataset** for 2layer CNN classifier using the FCGR and Bézier image generation methods.

The classification results for the DL model using the Human DNA dataset are given in Table 11 (in the appendix). We can observe that the pre-trained vision models and the vision transformer classifier are yielding very low performance corresponding to every image-based strategy. Again, it can be due to the gradient vanishing problem because of the small size of the dataset. Moreover, the custom CNN models are obtaining high performance, especially for the 1-layer CNN model and 2-layer CNN model. Note that increasing the number of layers in the custom CNN models reduces the performance, and a small dataset could be a reason for this behavior too. We can also notice that our proposed Bézier method is able to achieve performance in the top 5% for almost every evaluation metric corresponding to the custom CNN classifiers. Furthermore, the image-based methods clearly outperform the feature-engineering ones, hence indicating that converting the nucleotide sequences to images can retain more information about the sequences than mapping them to vectors in terms of classification predictive performance. Similarly, the String kernel method-based ML classifiers, except RF, also portray less performance than the custom CNN models, which yet again proves that converting sequences into images is more effective than mapping them to vectors.

## 5.5 SMILES String Dataset Performance

The classification results for the DL model using the SMILES String dataset are given in Table 12 (in the appendix). We can observe that the performance achieved by all the classifiers corresponding to every embedding strategy (image or vector) is very good and similar to each other, except for the DenseNet and EfficientNet models, which have bad results. A reason for the bad results could be the small size of the data, as DenseNet and EfficientNet usually operate on large datasets to have optimal performance. Note that although most of the classifiers portray similar results, our method achieves the maximum performance. Moreover, as this data contains sequences constituted of more than 20 unique characters, therefore, the FCGR & Spike2CGR methods failed to operate on them. Furthermore, our image-based method is performing better than the tabular

ones (feature-engineering-based and String kernel-based); hence, obtaining images of sequences is more useful for the classification.

## 5.6 Music Genre Dataset Performance

The classification results for the DL model using the Music Genre dataset are given in Table 13 (in the appendix). An important point to note here is that since the number of unique characters in the music data is  $> 20$ , the traditional FCGR and Spike2CGR methods fail to run on such datasets. In general, although the RandomCGR method performs better using classical vision models, the performance drastically reduces compared to the proposed method on the pre-trained vision models (e.g., see results for VGG-19 results in Table 13 (in the appendix) ). Such behavior supports our argument that, in general, the proposed method improves the performance of the pre-trained models in terms of sequence classification. Moreover, the image-based methods are clearly outperforming the feature-engineering and String-kernel baselines. Hence, image representations are more promising for classification than tabular ones.

## 5.7 t-SNE Data Visualization

We visualized the feature vectors using the t-SNE (t-distributed stochastic neighbor embedding) [22] approach extracted from the last hidden layer of the 2-layer CNN model for each of our datasets. The plots are computed for the images generated by the FCGR baseline and our proposed Bézier method.

The t-SNE visualization of FCGR and Bézier images of the protein subcellular localization dataset is illustrated in Figure 11 (in the appendix). We can clearly observe that the clusters generated corresponding to the Bézier data are very defined and visible. It indicates that the data structure is highly preserved even in 2D space due to the high quality of the respective embeddings used. As these embeddings are acquired from the images generated by our Bézier method, it implies that the images constructed by our method are of high quality and contain the sequence information efficiently and effectively. However, the t-SNE plot against the FCGR method consists of very overlapping and non-definite clusters, which indicates that the FCGR-based embeddings are unable to retain a good cluster structure in a low-dimensional space. Hence, they are suboptimal. Moreover, the t-SNE plots of the Coronavirus host dataset and ACP dataset are given in Appendix F.3 along with their respective discussions.

## 5.8 Confusion Matrix Results And Discussion

We investigated the confusion matrices obtained from the respective test sets of our host and protein subcellular datasets corresponding to the 2-layer CNN model for the FCGR baseline method and our proposed Bézier technique. We chose the 2-layer CNN classifier because it contains mostly the optimal predictive performance values for every dataset.

The confusion matrices corresponding to the protein subcellular localization dataset are illustrated in Figure 2. We can observe that our method is tremendously outperforming the FCGR baseline strategy as it has optimal true positive counts. Moreover, Bézier is also able to attain high performance for each category of the dataset. Overall, we can

witness that our method has almost perfect performance. Furthermore, the confusion matrices for other datasets are given in Appendix F.6.

## 6 Conclusion

In this work, we proposed a novel technique to convert biological sequences into images using the Bézier curve. It enables us to apply the sophisticated DL vision classifiers in the analysis of biological sequences. We validated our idea using three distinct protein datasets, and our method tremendously outperforms the baselines for protein subcellular localization classification and shows good performance on other dataset classifications. In the future, we want to explore the scalability of our technique by applying it to larger datasets. Moreover, we also want to investigate the generalizability of our method by using it on nucleotide-based datasets in future.

## References

1. Ali, S., Patterson, M.: Spike2vec: An efficient and scalable embedding approach for covid-19 spike sequences. In: International Conference on Big Data (Big Data). pp. 1533–1540 (2021)
2. Ali, S., Sahoo, B., Khan, M.A., Zelikovsky, A., Khan, I.U., Patterson, M.: Efficient approximate kernel based spike sequence classification. *IEEE/ACM Transactions on Computational Biology and Bioinformatics* (2022)
3. Baydas, S., Karakas, B.: Defining a curve as a bezier curve. *Journal of Taibah University for Science* **13**(1), 522–528 (2019)
4. Brandes, N., Ofer, D., Peleg, Y., Rappoport, N., Linial, M.: ProteinBERT: a universal deep-learning model of protein sequence and function. *Bioinformatics* **38**(8), 2102–2110 (02 2022). <https://doi.org/10.1093/bioinformatics/btac020>, <https://doi.org/10.1093/bioinformatics/btac020>
5. Farhan, M., Tariq, J., Zaman, A., Shabbir, M., Khan, I.: Efficient approximation algorithms for strings kernel based sequence classification. In: *Advances in neural information processing systems (NeurIPS)*. pp. 6935–6945. . (2017)
6. GISAID Website: <https://www.gisaid.org/> (2021), [Online; accessed 29-December-2021]
7. Grisoni, et al.: 'de novo design of anticancer peptides by ensemble artificial neural networks'. *Journal of Molecular Modeling* '25'('5'), '112' ('Apr' '2019'). <https://doi.org/10.1007/s00894-019-4007-6>, ' [WebLink]'
8. Hadfield, J., Megill, C., Bell, S., Huddleston, J., Potter, B., Callender, C., Sagulenko, P., Bedford, T., Neher, R.: Nextstrain: real-time tracking of pathogen evolution. *Bioinformatics* **34**, 4121–4123 (2018)
9. Han, X.A., Ma, Y., Huang, X.: A novel generalization of bézier curve and surface. *Journal of Computational and Applied Mathematics* **217**(1), 180–193 (2008)
10. He, K., Zhang, X., Ren, S., Sun, J.: Deep residual learning for image recognition. In: *IEEE conference on computer vision and pattern recognition*. pp. 770–778 (2016)
11. Heinzinger, M., Elnaggar, A., Wang, Y., Dallago, C., Nechaev, D., Matthes, F., Rost, B.: Modeling aspects of the language of life through transfer-learning protein sequences. *BMC bioinformatics* **20**(1), 1–17 (2019)

12. Hirokawa, T., Boon-Chiang, S., Mitaku, S.: Sosui: classification and secondary structure prediction system for membrane proteins. *Bioinformatics (Oxford, England)* **14**(4), 378–379 (1998)
13. Hug, R., Hübner, W., Arens, M.: Introducing probabilistic bézier curves for n-step sequence prediction. In: *Proceedings of the AAAI Conference on Artificial Intelligence*. vol. 34, pp. 10162–10169 (2020)
14. Human DNA: . In: <https://www.kaggle.com/code/nageshsingh/demystify-dna-sequencing-with-machine-learning/data>. pp. [Online; accessed 10–October–2022]
15. Iandola, F., Moskewicz, M., Karayev, S., Girshick, R., Darrell, T., Keutzer, K.: Densenet: Implementing efficient convnet descriptor pyramids. *arXiv preprint arXiv:1404.1869* (2014)
16. Jeffrey, H.J.: Chaos game representation of gene structure. *Nucleic acids research* **18**(8), 2163–2170 (1990)
17. Kuzmin, K., et al.: Machine learning methods accurately predict host specificity of coronaviruses based on spike sequences alone. *Biochemical and Biophysical Research Communications* **533**(3), 553–558 (2020)
18. Li, T., Ogihara, M., Li, Q.: A comparative study on content-based music genre classification. In: *Proceedings of the 26th annual international ACM SIGIR conference on Research and development in informaion retrieval*. pp. 282–289 (2003)
19. Liu, Y., Shen, C., Jin, L., He, T., Chen, P., Liu, C., Chen, H.: Abcnet v2: Adaptive bezier-curve network for real-time end-to-end text spotting. *IEEE Transactions on Pattern Analysis and Machine Intelligence* **44**(11), 8048–8064 (2021)
20. Löchel, H.F., Eger, D., Sperlea, T., Heider, D.: Deep learning on chaos game representation for proteins. *Bioinformatics* **36**(1), 272–279 (2020)
21. Ma, Y., Yu, Z., Tang, R., Xie, X., Han, G., Anh, V.V.: Phylogenetic analysis of hiv-1 genomes based on the position-weighted k-mers method. *Entropy* **22**(2), 255 (2020)
22. Van der Maaten, L., Hinton, G.: Visualizing data using t-sne. *Journal of machine learning research* **9**(11) (2008)
23. Minh, B.Q., et al.: Iq-tree 2: New models and efficient methods for phylogenetic inference in the genomic era. *Molecular Biology and Evolution* **37**(5), 1530–1534 (2020)
24. Murad, T., Ali, S., Khan, I., Patterson, M.: Spike2egr: an efficient method for spike sequence classification using chaos game representation. *Machine Learning* pp. 1–26 (2023)
25. Murad, T., Ali, S., Patterson, M.: A new direction in membranolytic anticancer peptides classification: Combining spaced k-mers with chaos game representation. *Procedia Computer Science* **222**, 666–675 (2023)
26. Pickett, B.E., Sadat, E.L., Zhang, Y., Noronha, J.M., Squires, R.B., Hunt, V., Liu, M., Kumar, S., Zaremba, S., Gu, Z., et al.: Vipr: an open bioinformatics database and analysis resource for virology research. *Nucleic acids research* **40**(D1), D593–D598 (2012)
27. Protein Subcellular Localization: <https://www.kaggle.com/datasets/lzyacht/proteinsubcellularlocalization> (2022), [Online; accessed 10–October–2022]
28. Qiao, L., Ding, W., Qiu, X., Zhang, C.: End-to-end vectorized hd-map construction with piecewise bezier curve. In: *Proceedings of the IEEE/CVF Conference on Computer Vision and Pattern Recognition*. pp. 13218–13228 (2023)
29. Rognan, D.: Chemogenomic approaches to rational drug design. *British journal of pharmacology* **152**(1), 38–52 (2007)
30. Shamay, Y., Shah, J., Işık, M., Mizrahi, A., Leibold, J., Tschaharganeh, D.F., Roxbury, D., Budhathoki-Uprety, J., Nawaly, K., Sugarman, J.L., et al.: Quantitative self-assembly prediction yields targeted nanomedicines. *Nature materials* **17**(4), 361–368 (2018)
31. Shen, J., Qu, Y., Zhang, W., Yu, Y.: Wasserstein distance guided representation learning for domain adaptation. In: *AAAI conference on artificial intelligence* (2018)

32. Simonyan, K., Zisserman, A.: Very deep convolutional networks for large-scale image recognition. In: International Conference on Learning Representations (2015)
33. Strodthoff, N., Wagner, P., Wenzel, M., Samek, W.: Udsmprot: universal deep sequence models for protein classification. *Bioinformatics* **36**(8), 2401–2409 (2020)
34. Tan, M., Le, Q.: Efficientnet: Rethinking model scaling for convolutional neural networks. In: International conference on machine learning. pp. 6105–6114. PMLR (2019)
35. Whisstock, J.C., Lesk, A.M.: Prediction of protein function from protein sequence and structure. *Quarterly reviews of biophysics* **36**(3), 307–340 (2003)
36. Xie, J., Girshick, R., Farhadi, A.: Unsupervised deep embedding for clustering analysis. In: International conference on machine learning. pp. 478–487 (2016)
37. Yao, et al.: Negative log likelihood ratio loss for deep neural network classification. In: Proceedings of the Future Technologies Conference. pp. 276–282. Springer (2019)
38. Zervou, M.A., Doutsis, E., Pavlidis, P., Tsakalides, P.: Structural classification of proteins based on the computationally efficient recurrence quantification analysis and horizontal visibility graphs. *Bioinformatics* **37**(13), 1796–1804 (2021)

## Appendix

### A Introduction

Figure 3 demonstrates the recursive procedures followed by CGR [16], FCGR [20], and protein secondary structure prediction [38] to allocate a location to nucleotides/amino acids in the corresponding generated images respectively.

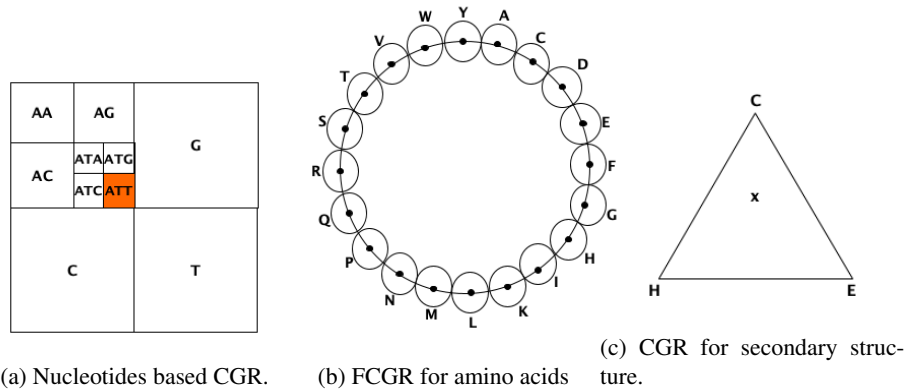


Fig. 3: Figure (a) shows the CGR-based determination of location for the "ATT" nucleotide sequence in the respective image. Figure (b) illustrates the 20-flakes-based image created using the FCGR method for a sequence of amino acids. (c) shows the CGR representation for the secondary protein structure.

### B Proposed Approach

Two example images generated by the Bézier curve-based method for two sequences (one from the active class and the other from the inactive class) from the ACP dataset are illustrated in Figure 4. We can observe that the created images are different from each other, which indicates that our method is able to preserve the information possessed by the sequences differently in the respective generated images.

### C Data Statistics

We have used 3 distinct protein sequence datasets to evaluate our proposed system. The details of each one are given as follows,

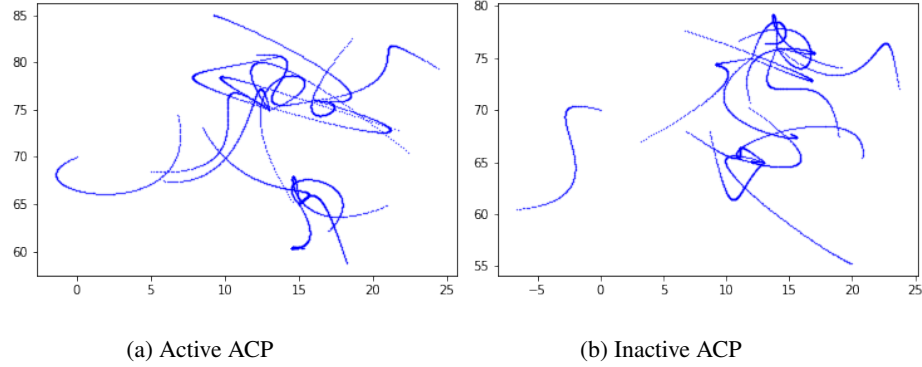


Fig. 4: The Bézier curve method-based images created for two sequences from the ACP dataset. One sequence belongs to the active class of the dataset, while the other is from the inactive class.

### C.1 Protein Subcellular Localization Dataset

This dataset [27] has 5959 unaligned protein sequences distributed among 11 unique subcellular locations. The associated subcellular location is predicted for a given protein sequence as input. The statistical details of the data are illustrated in Table 5.

Subcellular Locations	Count	Protein Subcellular Sequence Length		
		Min.	Max.	Average
Cytoplasm	1411	9	3227	337.32
Plasma Membrane	1238	47	3678	462.21
Extracellular Space	843	22	2820	194.01
Nucleus	837	16	1975	341.35
Mitochondrion	510	21	991	255.78
Chloroplast	449	71	1265	242.03
Endoplasmic Reticulum	198	79	988	314.64
Peroxisome	157	21	906	310.75
Golgi Apparatus	150	116	1060	300.70
Lysosomal	103	101	1744	317.81
Vacuole	63	60	607	297.95
Total	5959	-	-	-

Table 5: The protein subcellular localization dataset distribution with respect to the subcellular locations. The minimum, maximum, and average lengths of sequences belonging to each subcellular location are also mentioned.

## C.2 Coronavirus Host Dataset

The unaligned spike protein sequences from various clades of the Coronaviridae family are collected to form this dataset. It contains 5558 spike sequences, which are extracted from GISAID [6] and ViPR [26], accompanied with their respective infected host information. The sequences are distributed among 21 unique hosts. For the classification task, the infected host's name is determined based on a given spike sequence as an input. The statistical detail of this data is shown in Table 6. This data consists of spike protein sequences of the coronavirus and the reason for using only the spike protein region of the virus (rather than the full genome) is because it's well-known that major mutations happen in this region [17], possibly due to its ability to attach the virus to the host cell membrane. Figure 5 shows the full genome structure of the SARS-CoV-2 virus and "S" indicates the spike protein region.

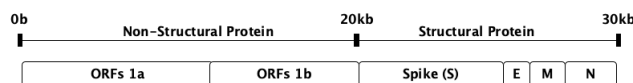


Fig. 5: The genome structure of SARS-CoV-2 virus.

## C.3 Anticancer Peptides (ACPs) Dataset

This dataset [7] consists of unaligned peptide-protein sequences along with their respective anticancer activity on the breast cancer cell lines. We utilize the sequences as inputs and their corresponding anticancer activity as target labels for classification. This data has 949 sequences distributed among the four unique target labels. The statistical detail of this data is given in Table 7.

## C.4 Human DNA Dataset

It consists of 2,000 unaligned Human DNA nucleotide sequences which are distributed among seven unique gene families. These gene families are used as labels for classification. The gene families are G Protein Coupled, Tyrosine Kinase, Tyrosine Phosphatase, Synthetase, Synthase, Ion Channel, and Transcription Factor containing 215, 299, 127, 347, 319, 94, & 599 instances respectively. The statistical detail of this data is given in Table 8.

## C.5 SMILES String

It has 6,568 SMILES strings distributed among ten unique drug subtypes extracted from the DrugBank dataset [30]. We employ the drug subtypes as a label for classification. The drug subtypes are Barbiturate [EPC], Amide Local Anesthetic [EPC],

Host	Count	Host Sequence Length		
		Min.	Max.	Average
Humans	1813	1154	1363	1273.63
Environment	1034	19	1276	1267.56
Weasel	994	9	1454	1270.69
Swines	558	1130	1573	1321.34
Birds	374	1153	1254	1166.93
Camels	297	1169	1366	1336.39
Bats	153	12	1399	1292.41
Cats	123	23	1467	1241.43
Bovines	88	1361	1584	1375.55
Canis	40	57	1473	1181.7
Rats	26	1126	1378	1314.42
Pangolins	21	10	1269	792.47
Hedgehog	15	1327	1363	1336.26
Dolphins	7	1482	1495	1486.85
Equine	5	1363	1363	1363.00
Fish	2	1190	1220	1205.0
Python	2	959	959	959.0
Monkey	2	1273	1273	1273.0
Unknown	2	1255	1271	1263.0
Turtle	1	922	922	922.0
Cattle	1	1169	1169	1169
Total	5558	-	-	-

Table 6: The distribution of spike protein sequences among the infected hosts. The minimum, maximum, and average lengths of sequences belonging to each host are also mentioned.

ACPs Class	Count	Peptide Sequence Length		
		Min.	Max.	Average
Inactive-Virtual	750	8	30	16.64
Moderate Active	98	10	38	18.44
Inactive-Experimental	83	5	38	15.02
Very Active	18	13	28	19.33
Total	949	-	-	-

Table 7: ACPs dataset distribution based on their respective activity on the breast cancer cell line. The minimum, maximum, and average lengths of sequences belonging to each class are also mentioned.

Non-Standardized Plant Allergenic Extract [EPC], Sulfonylurea [EPC], Corticosteroid [EPC], Nonsteroidal Anti-inflammatory Drug [EPC], Nucleoside Metabolic Inhibitor [EPC], Nitroimidazole Antimicrobial [EPC], Muscle Relaxant [EPC], and Others with 54, 53, 30, 17, 16, 15, 11, 10, 10, & 6, 352 instances respectively. The statistical detail of this data is given in Table 9.

Gene Family	Count	DNA Sequence Length		
		Min.	Max.	Average
G Protein Coupled	215	30	18921	1859.04
Tyrosine Kinase	299	24	4863	1509.64
Tyrosine Phosphatase	127	135	7473	2486.14
Synthetase	347	8	3795	965.30
Synthase	319	31	7536	899.63
Ion Channel	94	42	5598	1949.809
Transcription Factor	599	9	9141	1152.85
Total	2000	-	-	-

Table 8: Human DNA dataset distribution based on their gene family type. The minimum, maximum, and average lengths of sequences belonging to each class are also mentioned.

Gene Family	Count	DNA Sequence Length		
		Min.	Max.	Average
Barbiturate [EPC]	54	16	136	51.24
Amide Local Anesthetic [EPC]	53	9	149	39.18
Non-Standardized Plant Allergenic Extract [EPC]	30	10	255	66.89
Sulfonylurea [EPC]	17	22	148	59.76
Corticosteroid [EPC]	16	57	123	95.43
Nonsteroidal Anti-inflammatory Drug [EPC]	15	29	169	53.6
Nucleoside Metabolic Inhibitor [EPC]	11	16	145	59.90
Nitroimidazole Antimicrobial [EPC]	10	27	147	103.8
Muscle Relaxant [EPC]	10	9	82	49.8
Others	6352	2	569	55.44
Total	6568	-	-	-

Table 9: SMILES String dataset distribution based on their drug subtype. The minimum, maximum, and average lengths of sequences belonging to each class are also mentioned.

### C.6 Music Dataset

This data has 1,000 audio sequences belonging to 10 unique music genres, where each genre contains 100 sequences [18]. We perform music genre classification tasks using this dataset. The genres are Blues, Classical, Country, Disco, Hiphop, Jazz, Metal, Pop, Reggae, and Rock. The statistical detail of this data is given in Table 10.

## D Baseline Models

The details of each of the baseline methods used to perform the evaluation are as follows,

Genre	Count	Music Sequence Length		
		Min.	Max.	Average
Blues	100	6892	6892	6892.00
Classical	100	6887	7001	6895.36
Country	100	6885	6974	6894.44
Disco	100	6887	6958	6893.49
Hiphop	100	6889	6889	6889.00
Jazz	100	6873	7038	6909.45
Metal	100	6891	6999	6896.57
Pop	100	6889	6892	6889.96
Reggae	100	6889	6892	6890.23
Rock	100	6888	6981	6894.26
Total	1000	-	-	-

Table 10: Music dataset distribution based on their genre. The minimum, maximum, and average lengths of sequences belonging to each class are also mentioned.

### D.1 One-Hot Encoding (OHE)

This technique is employed to convert the sequential data into numerical format [17]. For each character within the sequence, a binary vector is associated with it and then all these vectors are combined to form a comprehensive representation of the entire sequence. While OHE is a straightforward approach, it yields vectors that are notably sparse, where most of the elements are zero. This phenomenon is commonly called the "curse of dimensionality," which presents challenges due to the substantial increase in dimensions relative to the available data points.

### D.2 Wasserstein Distance Guided Representation Learning (WDGRL)

This domain adaption method is used for adapting data from one domain to another [31]. Its core focus is evaluating the Wasserstein distance (WD) between the encoded distributions of the source and target domains. To achieve it, a neural network is employed. It transforms high-dimensional data into low dimensions. It's worth noting that WDGRL builds upon the feature vectors that are initially generated using the One-Hot Encoding (OHE) technique. However, as it needs large training data to obtain optimal features, therefore it's an expensive mechanism.

### D.3 Frequency Chaos Game Representation (FCGR)

FCGR is specifically designed to map protein sequences into images based on the concept of Chaos Game Representation (CGR) [16]. For a given protein sequence, it constructs an  $n$ -flakes-based image, which consists of multiple icosagons, and  $n$  represents the number of amino acids in the sequence [20]. For an amino acid, the corresponding pixel coordinates are determined using the following equations,

$$x = r \cdot \sin\left(\frac{2\pi i}{n} + \theta\right) \quad (4)$$

$$y = r \cdot \cos\left(\frac{2\pi i}{n} + \theta\right) \quad (5)$$

where  $r$  contraction ratio between the outer and inner polygons.

#### D.4 Random Chaos Game Representation (RandomCGR)

This method follows a random function to determine the pixel coordinates for an amino acid in the corresponding image representation [25]. These coordinates are further connected with the location axis of the previous amino acid to represent the existing amino acid in the image.

Furthermore, an example of images generated for a sequence taken from the Coronavirus host dataset's bat class against our proposed method and the image-based baseline models is shown in Figure 6. Moreover, the sample images from other datasets are given in Figure 7 Figure 8 Figure 9. We can observe that the constructed images are distinct for each method, which indicates that every image-creating method is able to have different modeling of the information from the sequence in the respective visual form. Hence, every method will achieve different performance in terms of classification.

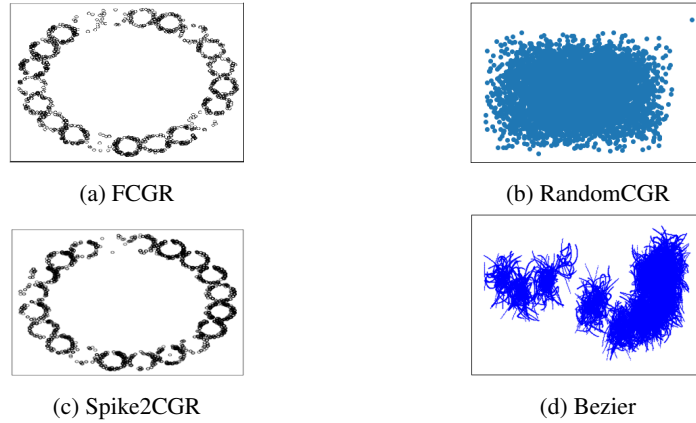


Fig. 6: The example of images created by our proposed Bézier curve-based method and the image-based baselines methods (FCGR, RandomCGR & Spike2CGR) for a randomly selected sequence from the **Coronavirus host** dataset.

## E Experimental Evaluation

### E.1 Evaluation Metrics

Various evaluation metrics are employed by us to analyze the performance of the classification models. Those metrics are average accuracy, precision, recall, F1 (weighted), F1 (macro), and ROC AUC. As our classification problems are multi-class, therefore

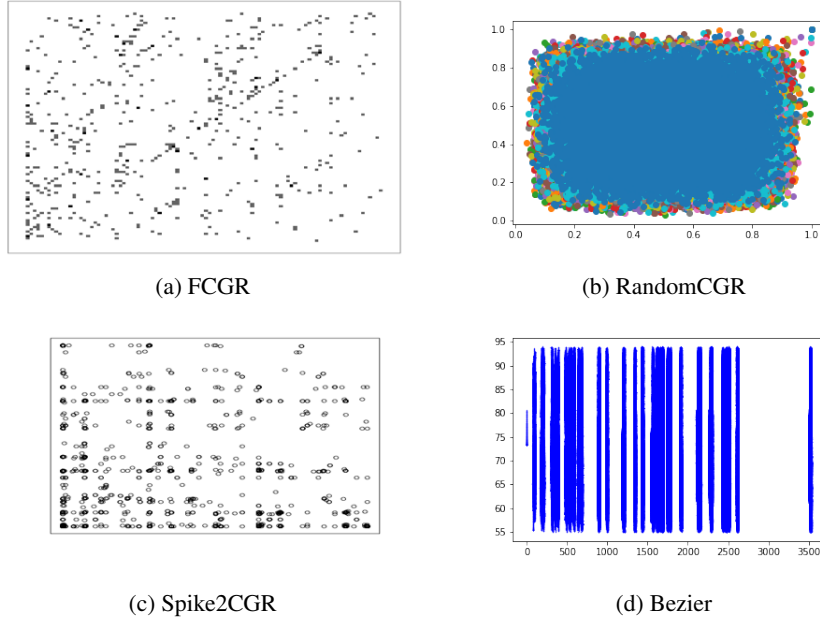


Fig. 7: The example of images created by our proposed Bézier curve-based method and the image-based baselines methods (FCGR, RandomCGR & Spike2CGR) for a randomly selected sequence from the **Human DNA dataset**.

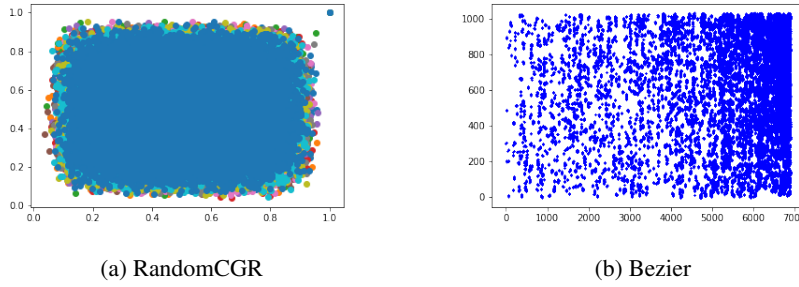


Fig. 8: The example of images created by our proposed Bézier curve-based method and the image-based baselines methods (FCGR, RandomCGR & Spike2CGR) for a randomly selected sequence from the **Music dataset**.

we utilized the one-vs-rest approach for computing the ROC AUC score. The reported values for any metric are an average of 5 runs. Moreover, several metrics are used to obtain deeper insights into the performance of the classifiers, especially because our datasets are undergoing the data imbalance challenge.

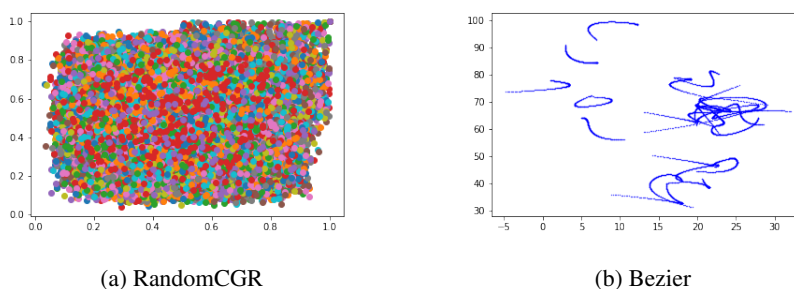


Fig. 9: The example of images created by our proposed Bézier curve-based method and the image-based baselines methods (FCGR, RandomCGR & Spike2CGR) for a randomly selected sequence from the **SMILES String dataset**.

**Image Models** These models are used for image-based classification. We construct four custom convolutional neural networks (CNNs) classifiers with varying numbers of hidden layers to do the classification tasks. These models are referred to as 1-layer, 2-layer, 3-layer & 4-layer CNN classifiers, and they consist of 1, 2, 3, & 4 hidden block A modules respectively. A block A module contains a convolution layer followed by a ReLU activation function and a max-pool layer. Each convolution layer uses kernel and stride filters of size  $5 \times 5$  &  $2 \times 2$ , respectively. The max-pooling layer is also accompanied by the kernel and stride filters of  $2 \times 2$  sizes for both. For each classifier, the block A modules are followed by two fully connected layers and a Softmax classification layer. The architecture of the 1-layer CNN model is illustrated in Figure 10. These custom CNN networks are employed to investigate the impact of increasing the number of hidden layers on the final predictive performance.

Moreover, a vision transformer model (ViT) is also used by us for performing the classification tasks. As ViT is known to utilize the power of transformer architecture, we want to see its impact on our bio-sequence datasets classifications. In ViT the input image is partitioned into patches, which are then linearly transformed into vectors by a linear embedding module. Note that we used patch size 20 & 8 vector dimensions in our experiments. Then positional embeddings are added to the vectors and they are subsequently processed by two Transformer encoder blocks. Each encoder block consists of a normalization layer, a multi-head self-attention layer with residual connections, a second normalization layer, and a multi-layer perceptron with another residual connection. The final output is directed to a softmax classification module for image label prediction. This design capitalizes on self-attention mechanisms for efficient image classification.

Furthermore, we also examine the consequences of using pre-trained vision models for classifying our datasets, and for that, we used pre-trained ResNet-50 [10], EfficientNet [34], DenseNet [15] and VGG19 [32] models. Moreover, all the generated images for any dataset are of dimensions  $720 \times 480$ , and they are given as input to the image-based classifiers. The hyperparameters decided after fine-tuning are 0.003 learning rate, ADAM optimizer, 64 batch size, and 10 training epochs for all the models. Addition-

ally, the negative log-likelihood (NLL) [37] loss function is employed for training, as it's known to be a cross-entropy loss function for multi-class problems.

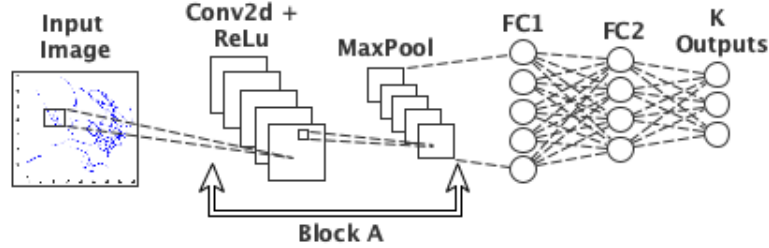


Fig. 10: The architecture of 1-layer CNN model. For a given input image, it yields the K classification classes as output.

## F Results and Discussion

### F.1 Coronavirus Host Dataset's Performance

The Coronavirus host dataset-based classification performance via various evaluation metrics is reported in Table 14.

The results demonstrate that, overall, the Bezier-based images show promising performance for the host classification task. Among the image-based baselines, it portrays a very comparable performance with the FCGR baseline and has outperformed the RandomCGR method. Moreover, the image representations are clearly performing better than the tabular ones (feature-engineering methods based). Hence, converting the spike protein sequences of the Coronavirus into images is more effective for performing classification than transforming them into numerical vectors (tabular form).

### F.2 ACP Dataset's Performance

The classification performance achieved using the ACP dataset for various evaluation metrics is summarized in Table 15.

We can observe that, among the image-based baseline approaches, Bezier is showcasing very comparable performance as the FCGR because most of the top 5% scores corresponding to various evaluation metrics are falling against these methods. Moreover, Bezier is clearly outperforming the RandomCGR baseline. Although the OHE method exhibits high performance for some of the evaluation metrics, generally, the feature engineering methods have lower predictive performance than the image-based ones. Overall, we can say that the Bezier method portrays promising results for the ACP classification task, which implies that converting the ACP sequences into images using the Bezier method is effective in terms of classification performance.

Category	DL Model	Method	Acc. ↑	Prec. ↑	Recall ↑	F1 (Weig.) ↑	F1 (Macro) ↑	ROC AUC ↑	Train Time (hrs.) ↓
Tabular Models	3-Layer	OHE	0.627	0.699	0.627	0.613	0.566	0.729	0.024
	Tab CNN	WDGRL	0.657	0.716	0.657	0.649	0.601	0.758	0.020
	4-Layer	OHE	0.680	0.704	0.680	0.661	0.581	0.762	0.042
	Tab CNN	WDGRL	0.654	0.692	0.654	0.635	0.551	0.743	0.038
String Kernel	-	SVM	0.618	0.617	0.618	0.613	0.588	0.753	39.791
	-	NB	0.338	0.452	0.338	0.347	0.333	0.617	0.276
	-	MLP	0.597	0.595	0.597	0.593	0.549	0.737	331.068
	-	KNN	0.645	0.657	0.645	0.646	0.612	0.774	1.274
	-	RF	0.731	0.776	0.731	0.729	0.723	0.808	12.673
	-	LR	0.571	0.570	0.571	0.558	0.532	0.716	2.995
	-	DT	0.630	0.631	0.630	0.630	0.598	0.767	2.682
Custom CNN Models	1-Layer	FCGR	0.717	0.719	0.717	0.709	0.711	0.834	0.351
		RandmCGR	0.820	0.827	0.820	0.816	0.787	0.872	0.355
		Spike2CGR	0.662	0.698	0.662	0.660	0.627	0.768	0.353
		Bézier	0.710	0.712	0.710	0.700	0.713	0.831	0.339
	% impro. of Bézier from Spike2CGR		5.1	1.4	5.1	4	8.6	6.3	-3.9
	2-Layer	FCGR	0.705	0.708	0.705	0.694	0.691	0.831	0.365
		RandmCGR	0.785	0.791	0.785	0.782	0.750	0.845	0.622
		Spike2CGR	0.665	0.685	0.665	0.664	0.633	0.786	0.692
		Bézier	0.700	0.722	0.700	0.695	0.659	0.803	0.350
	% impro. of Bézier from Spike2CGR		3.5	3.7	3.5	3.1	2.6	1.7	49.4
3-Layer	FCGR	0.632	0.641	0.632	0.623	0.609	0.767	0.332	
	RandmCGR	0.710	0.724	0.710	0.697	0.661	0.807	0.530	
	Spike2CGR	0.580	0.636	0.580	0.582	0.514	0.715	0.331	
	Bézier	0.426	0.498	0.426	0.351	0.298	0.594	0.376	
% impro. of Bézier from Spike2CGR		-15.4	-13.8	-15.4	-23.1	-21.6	-12.1	-13.59	
4-Layer	FCGR	0.300	0.090	0.300	0.138	0.065	0.500	0.331	
	RandmCGR	0.287	0.082	0.287	0.128	0.063	0.500	0.521	
	Spike2CGR	0.377	0.385	0.377	0.305	0.232	0.562	0.311	
	Bézier	0.313	0.097	0.313	0.149	0.068	0.500	0.321	
% impro. of Bézier from Spike2CGR		-6.4	-28.8	-6.4	-15.6	-16.4	-6.2	-3.2	
Vision Transformer	ViT	FCGR	0.300	0.090	0.300	0.138	0.065	0.500	0.782
		RandmCGR	0.295	0.140	0.295	0.142	0.097	0.510	0.828
		Spike2CGR	0.307	0.094	0.307	0.144	0.067	0.500	3.787
		Bézier	0.382	0.326	0.382	0.323	0.239	0.613	0.654
	% impro. of Bézier from Spike2CGR		7.5	23.2	7.5	17.9	17.2	11.3	82.7
ResNet-50	ResNet-50	FCGR	0.357	0.251	0.357	0.283	0.208	0.500	0.495
		RandmCGR	0.290	0.192	0.290	0.137	0.072	0.500	0.481
		Spike2CGR	0.352	0.341	0.352	0.295	0.208	0.565	2.443
		Bézier	0.408	0.244	0.408	0.294	0.184	0.561	0.873
	% impro. of Bézier from Spike2CGR		5.6	-9.7	5.6	-0.1	-2.4	-0.4	64.2
VGG-19	VGG-19	FCGR	0.345	0.285	0.345	0.249	0.181	0.540	1.078
		RandmCGR	0.287	0.082	0.287	0.128	0.063	0.500	1.115
		Spike2CGR	0.307	0.094	0.307	0.144	0.067	0.500	3.032
		Bézier	0.317	0.132	0.317	0.176	0.098	0.510	1.221
	% impro. of Bézier from Spike2CGR		1	3.8	1	3.2	3.1	1	59.7
DenseNet	DenseNet	FCGR	0.075	0.005	0.075	0.010	0.019	0.500	0.764
		RandmCGR	0.062	0.003	0.062	0.007	0.016	0.500	0.825
		Spike2CGR	0.067	0.004	0.067	0.008	0.018	0.500	1.295
		Bézier	0.078	0.007	0.078	0.013	0.022	0.491	0.822
	% impro. of Bézier from Spike2CGR		1.1	0.3	1.1	0.5	0.4	-0.9	36.5
EfficientNet	EfficientNet	FCGR	0.200	0.141	0.200	0.147	0.094	0.517	0.814
		RandmCGR	0.287	0.082	0.287	0.128	0.063	0.500	0.837
		Spike2CGR	0.275	0.169	0.275	0.187	0.112	0.524	1.343
		Bézier	0.313	0.097	0.313	0.149	0.068	0.500	0.844
	% impro. of Bézier from Spike2CGR		3.8	-7.2	3.8	-3.8	-4.4	-2.4	37.1

Table 11: Classification results for different models and algorithms for **Human DNA dataset**. The top 5% values for each metric are underlined.

Category	DL Model	Method	Acc. $\uparrow$	Prec. $\uparrow$	Recall $\uparrow$	F1 (Weig.) $\uparrow$	F1 (Macro) $\uparrow$	ROC AUC $\uparrow$	Train Time (hrs.) $\downarrow$	
Tabular Models	3-Layer	OHE	0.966	0.935	0.966	0.950	0.098	0.500	0.132	
	Tab CNN	WDGRL	0.966	0.935	0.966	0.950	0.098	0.500	<u>0.001</u>	
	4-Layer	OHE	0.966	0.935	0.966	0.950	0.098	0.500	0.155	
	Tab CNN	WDGRL	0.966	0.935	0.966	0.950	0.098	0.500	<u>0.001</u>	
String Kernel	-	SVM	0.812	0.813	0.812	0.811	0.084	0.502	10.254	
	-	NB	0.537	0.643	0.537	0.549	0.096	0.502	<u>1.24</u>	
	-	MLP	0.789	0.788	0.789	0.790	0.079	0.505	13.149	
	-	KNN	0.844	0.858	0.844	0.842	0.087	0.503	2.348	
	-	RF	0.929	0.927	0.929	0.925	0.098	0.507	9.315	
	-	LR	0.772	0.769	0.772	0.760	0.073	0.502	5.652	
	-	DT	0.834	0.829	0.834	0.832	0.075	<u>0.508</u>	3.318	
Custom CNN Models	1-Layer	RandmCGR	0.962	0.926	0.962	0.944	0.098	0.500	0.988	
		Bézier	<u>0.970</u>	<u>0.942</u>	<u>0.970</u>	<u>0.956</u>	<u>0.109</u>	<u>0.512</u>	1.003	
	% impro. of Bézier from RandmCGR		0.8	1.6	0.8	1.2	1.1	12	-1.51	
	2-Layer	RandmCGR	0.962	0.926	0.962	0.944	0.098	0.500	0.989	
		Bézier	<u>0.970</u>	<u>0.942</u>	<u>0.970</u>	<u>0.956</u>	<u>0.109</u>	<u>0.512</u>	1.253	
	% impro. of Bézier from RandmCGR		0.8	1.6	0.8	1.2	1.1	12	-26.6	
	3-Layer	RandmCGR	0.962	0.926	0.962	0.944	0.098	0.500	1.411	
		Bézier	<u>0.970</u>	<u>0.942</u>	<u>0.970</u>	<u>0.956</u>	<u>0.109</u>	0.511	1.082	
	% impro. of Bézier from RandmCGR		0.8	1.6	0.8	1.2	1.1	12	80.04	
	4-Layer	RandmCGR	0.962	0.926	0.962	0.944	0.098	0.500	1.331	
		Bézier	<u>0.970</u>	<u>0.942</u>	<u>0.970</u>	<u>0.956</u>	<u>0.109</u>	<u>0.512</u>	1.210	
	% impro. of Bézier from RandmCGR		0.8	1.6	0.8	1.2	1.1	12	9.09	
	Vision Transformer	ViT	RandmCGR	0.962	0.926	0.962	0.944	0.098	0.500	1.876
			Bézier	<u>0.970</u>	<u>0.942</u>	<u>0.970</u>	<u>0.956</u>	<u>0.109</u>	<u>0.512</u>	1.864
% impro. of Bézier from RandmCGR		0.8	1.6	0.8	1.2	1.1	12	0.63		
Pretrained Vision Models	ResNet-50	RandmCGR	0.962	0.926	0.962	0.944	0.098	0.500	1.872	
		Bézier	<u>0.970</u>	0.940	<u>0.970</u>	0.950	0.100	0.500	1.142	
	% impro. of Bézier from RandmCGR		0.8	1.4	0.8	0.6	0.2	0	38.99	
	VGG-19	RandmCGR	0.962	0.926	0.962	0.944	0.098	0.500	7.120	
		Bézier	<u>0.970</u>	0.940	<u>0.970</u>	0.950	0.100	0.500	2.899	
	% impro. of Bézier from RandmCGR		0.8	1.4	0.8	0.6	0.2	0	59.2	
	DenseNet	RandmCGR	0.001	0.024	0.001	0.004	0.000	0.500	5.043	
		Bézier	0.001	0.023	0.001	0.066	0.000	0.500	2.867	
	% impro. of Bézier from RandmCGR		0	1	0	6.2	0	0	43.14	
	EfficientNet	RandmCGR	0.962	0.926	0.962	0.944	0.098	0.500	4.892	
Bézier		0.969	0.938	0.969	0.950	0.100	0.500	3.892		
% impro. of Bézier from RandmCGR		0.6	1.2	0.6	5.6	0.2	0	20.44		

Table 12: Classification results for different models and algorithms for **SMILES String dataset**. The best value for each metric is underlined. As the performances of most of the models are the same and highlighting the top 5% includes a lot of data, that’s why we only underlined the best one.

Category	DL Model	Method	Acc. ↑	Prec. ↑	Recall ↑	F1 (Weig.) ↑	F1 (Macro) ↑	ROC AUC ↑	Train Time (hrs.) ↓
Tabular Models	3-Layer	OHE	0.515	0.682	0.515	0.611	0.451	0.652	<u>0.003</u>
	Tab CNN	WDGRL	0.599	0.600	0.599	0.565	0.515	0.659	<u>0.001</u>
	4-Layer	OHE	0.516	0.555	0.516	0.511	0.451	0.652	<u>0.003</u>
	Tab CNN	WDGRL	0.612	0.588	0.612	0.588	0.530	0.670	<u>0.001</u>
String Kernel	-	SVM	0.301	0.322	0.301	0.294	0.294	0.615	0.886
	-	NB	0.369	0.376	0.369	0.357	0.352	0.649	<u>0.039</u>
	-	MLP	0.219	0.231	0.219	0.212	0.211	0.568	3.476
	-	KNN	0.400	0.409	0.400	0.388	0.387	0.669	0.169
	-	RF	0.341	0.354	0.341	0.334	0.333	0.638	1.478
	-	LR	0.397	0.397	0.397	0.389	0.386	0.666	21.209
	-	DT	0.283	0.290	0.283	0.282	0.281	0.603	0.392
Custom CNN Models	1-Layer	RandmCGR	<u>0.989</u>	<u>0.989</u>	<u>0.989</u>	<u>0.989</u>	<u>0.989</u>	<u>0.989</u>	0.400
		Bézier	<u>0.957</u>	<u>0.953</u>	<u>0.957</u>	<u>0.953</u>	<u>0.844</u>	<u>0.919</u>	0.312
		% improv. of Bézier from RandomCGR	-3.2	-3.6	-3.2	-3.6	-14.5	-7	22
	2-Layer	RandmCGR	<u>0.985</u>	<u>0.985</u>	<u>0.985</u>	<u>0.985</u>	<u>0.985</u>	<u>0.992</u>	0.4121
		Bézier	<u>0.943</u>	<u>0.941</u>	<u>0.943</u>	<u>0.939</u>	<u>0.827</u>	<u>0.911</u>	0.345
		% improv. of Bézier from RandomCGR	-4.2	-4.3	-4.2	-4.6	-15.8	-1.1	16.2
	3-Layer	RandmCGR	0.085	0.007	0.085	0.013	0.015	0.500	0.541
		Bézier	0.886	0.893	0.886	0.882	0.789	0.887	0.453
		% improv. of Bézier from RandomCGR	80.1	88.6	80.1	86.9	77.4	38.7	16.2
	4-Layer	RandmCGR	0.155	0.044	0.155	0.063	0.074	0.545	0.554
		Bézier	<u>0.900</u>	<u>0.908</u>	<u>0.900</u>	<u>0.897</u>	<u>0.802</u>	<u>0.895</u>	0.438
		% improv. of Bézier from RandomCGR	74.5	86.4	74.5	83.4	72.8	35	20.9
Vision Transformer	ViT	RandmCGR	0.110	0.012	0.110	0.021	0.019	0.500	0.807
		Bézier	0.099	0.009	0.099	0.017	0.022	0.500	1.090
		% improv. of Bézier from RandomCGR	-1.1	-0.3	-1.1	-0.4	-0.3	0	-23.9
Pretrained Vision Models	ResNet-50	RandmCGR	0.525	0.608	0.525	0.485	0.496	0.740	0.653
		Bézier	0.546	0.545	0.546	0.479	0.457	0.728	0.543
		% improv. of Bézier from RandomCGR	2.1	-6.3	2.1	0.6	-3.9	-1.2	16.8
	VGG-19	RandmCGR	0.410	0.421	0.410	0.334	0.410	0.673	1.220
		Bézier	0.843	0.867	0.843	0.838	0.741	0.856	1.421
		% improv. of Bézier from RandomCGR	43.3	44.6	43.3	50.4	33.1	18.3	-16.47
	DenseNet	RandmCGR	0.080	0.056	0.080	0.052	0.053	0.489	2.118
		Bézier	0.113	0.130	0.113	0.043	0.049	0.508	2.332
		% improv. of Bézier from RandomCGR	3.3	7.4	3.3	-0.9	-0.4	1.9	-10.10
	EfficientNet	RandmCGR	0.735	0.719	0.735	0.697	0.689	0.851	1.011
	Bézier	0.929	0.928	0.929	0.924	0.808	0.898	0.889	
	% improv. of Bézier from RandomCGR	19.4	20.9	19.4	22.7	11.9	4.7	12.06	

Table 13: Classification results for different models and algorithms for **Music Genre dataset**. The top 5% values for each metric are underlined.

### F.3 t-SNE Data Visualization

The t-SNE plots for the Coronavirus host dataset are shown in Figure 12. We can observe that the clusters generated by both FCGR and Bézier are very scattered and over-

Category	DL Model	Method	Acc. $\uparrow$	Prec. $\uparrow$	Recall $\uparrow$	F1 (Weig.) $\uparrow$	F1 (Macro) $\uparrow$	ROC AUC $\uparrow$	Train Time (hrs.) $\downarrow$	
Tabular Models	3-Layer	OHE	0.625	0.626	0.625	0.566	0.335	0.663	<u>0.032</u>	
	Tab CNN	WDGRL	0.304	0.137	0.304	0.182	0.041	0.499	<u>0.029</u>	
	4-Layer	OHE	0.613	0.478	0.613	0.534	0.323	0.662	<u>0.067</u>	
	Tab CNN	WDGRL	0.312	0.130	0.312	0.167	0.035	0.498	<u>0.054</u>	
String Kernel	-	SVM	0.601	0.673	0.601	0.602	0.325	0.624	5.198	
	-	NB	0.230	0.665	0.230	0.295	0.162	0.625	<u>0.131</u>	
	-	MLP	0.647	0.696	0.647	0.641	0.302	0.628	42.322	
	-	KNN	0.613	0.623	0.613	0.612	0.310	0.629	0.434	
	-	RF	<u>0.668</u>	0.692	<u>0.668</u>	0.663	0.360	0.658	4.541	
	-	LR	0.554	<u>0.724</u>	0.554	0.505	0.193	0.568	5.096	
	-	DT	0.646	0.674	0.646	0.643	0.345	0.653	1.561	
Custom CNN Models	1-Layer	FCGR	0.680	<u>0.707</u>	0.680	<u>0.670</u>	0.517	0.761	0.984	
		Spike2CGR	<u>0.743</u>	<u>0.745</u>	<u>0.743</u>	<u>0.739</u>	<u>0.569</u>	<u>0.797</u>	0.711	
		RandomCGR	0.262	0.193	0.262	0.210	0.051	0.500	8.695	
		Bézier	0.652	0.652	0.652	0.644	<u>0.592</u>	<u>0.766</u>	2.698	
	% improv. of FCGR		of Bézier from -2.8		-5.5	-2.8	-2.6	7.5	0.5	-174.18
	2-Layer	FCGR	<u>0.668</u>	0.684	<u>0.668</u>	0.655	0.410	0.710	1.046	
		Spike2CGR	<u>0.740</u>	<u>0.734</u>	<u>0.740</u>	<u>0.726</u>	0.428	0.716	0.688	
		RandomCGR	0.293	0.235	0.293	0.246	0.093	0.521	8.839	
		Bézier	0.656	0.669	0.656	0.644	<u>0.610</u>	<u>0.778</u>	2.976	
	% improv. of FCGR		of Bézier from -1.2		-1.5	-1.2	-1.1	20	6.8	-184.51
	3-Layer	FCGR	0.681	0.677	0.681	<u>0.672</u>	0.470	0.740	5.681	
		Spike2CGR	<u>0.729</u>	<u>0.729</u>	<u>0.729</u>	<u>0.715</u>	0.354	0.677	0.831	
		RandomCGR	0.320	0.102	0.320	0.155	0.028	0.500	9.440	
		Bézier	0.611	0.652	0.611	0.612	<u>0.623</u>	<u>0.793</u>	4.660	
	% improv. of FCGR		of Bézier from -7		-2.5	-7	-6	15.3	5.3	17.97
	4-Layer	FCGR	0.624	0.617	0.624	0.606	0.262	0.623	8.991	
Spike2CGR		0.686	0.668	0.686	<u>0.672</u>	0.283	0.632	0.684		
RandomCGR		0.320	0.102	0.320	0.155	0.028	0.500	10.778		
Bézier		0.640	0.643	0.640	0.575	<u>0.594</u>	<u>0.782</u>	5.102		
% improv. of FCGR		of Bézier from 1.6		2.6	1.6	-3.1	33.2	15.9	43.25	
Vision Transformer	ViT	FCGR	0.322	0.104	0.322	0.157	0.023	0.500	0.188	
		Spike2CGR	0.332	0.323	0.332	0.333	0.213	0.500	0.877	
		RandomCGR	0.320	0.102	0.320	0.155	0.028	0.500	0.173	
		Bézier	0.316	0.100	0.316	0.152	0.022	0.500	0.183	
	% improv. of FCGR		of Bézier from -0.6		-0.4	-0.6	-0.5	-0.1	0	2.65
ResNet-50	FCGR	0.662	0.665	0.662	0.639	0.267	0.621	8.840		
	Spike2CGR	<u>0.691</u>	0.683	<u>0.691</u>	0.663	0.270	0.624	0.786		
	RandomCGR	0.319	0.113	0.319	0.159	0.030	0.500	13.488		
	Bézier	0.571	0.473	0.571	0.504	0.335	0.564	6.411		
% improv. of FCGR		of Bézier from -9.1		-19.2	-9.1	-13.5	6.8	-5.7	27.47	
Pretrained Vision Models	VGG-19	FCGR	0.519	0.475	0.519	0.442	0.158	0.572	3.738	
		Spike2CGR	0.458	0.409	0.458	0.363	0.129	0.559	3.409	
		RandomCGR	0.320	0.102	0.320	0.155	0.028	0.500	21.474	
		Bézier	0.521	0.421	0.521	0.448	0.222	0.500	3.200	
	% improv. of FCGR		of Bézier from 0.2		-5.4	0.2	0.6	6.4	-7.2	14.39
DenseNet	FCGR	0.018	0.000	0.018	0.001	0.018	0.500	2.566		
	Spike2CGR	0.017	0.000	0.017	0.000	0.001	0.500	2.675		
	RandomCGR	0.015	0.000	0.015	0.000	0.001	0.500	2.123		
	Bézier	0.011	0.000	0.011	0.001	0.011	0.500	2.332		
% improv. of FCGR		of Bézier from -0.8		0	-0.8	0	-0.8	0	9.11	
EfficientNet	FCGR	0.169	0.028	0.169	0.049	0.013	0.500	34.443		
	Spike2CGR	0.169	0.031	0.169	0.053	0.015	0.500	31.229		
	RandomCGR	0.317	0.108	0.317	0.162	0.032	0.529	37.334		
	Bézier	0.465	0.427	0.465	0.394	0.157	0.577	35.768		
% improv. of FCGR		of Bézier from 29.6		39.9	29.6	34.5	14.4	7.7	-3.84	

Table 14: Classification results for different models and algorithms for **Coronavirus Host dataset**. The top 5% values for each metric are underlined.

Category	DL Model	Method	Acc. $\uparrow$	Prec. $\uparrow$	Recall $\uparrow$	F1 (Weig.) $\uparrow$	F1 (Macro) $\uparrow$	ROC AUC $\uparrow$	Train Time (hrs.) $\downarrow$	
Tabular Models	3-Layer Tab CNN	OHE	0.768	<u>0.839</u>	0.768	0.790	<u>0.452</u>	<u>0.719</u>	<u>0.042</u>	
		WDGRL	0.615	<u>0.740</u>	0.615	0.660	0.326	0.603	<u>0.0001</u>	
	4-Layer Tab CNN	OHE	0.796	<u>0.843</u>	0.796	<u>0.807</u>	<u>0.474</u>	<u>0.736</u>	<u>0.056</u>	
		WDGRL	0.631	0.754	0.631	0.673	0.346	0.623	<u>0.0002</u>	
String Kernel	-	SVM	0.802	0.836	0.802	0.813	0.454	0.692	0.789	
	-	NB	<u>0.872</u>	<u>0.869</u>	<u>0.872</u>	0.864	<u>0.523</u>	<u>0.732</u>	<u>0.018</u>	
	-	MLP	0.611	0.771	0.611	0.666	0.348	0.626	2.478	
	-	KNN	<u>0.871</u>	<u>0.849</u>	<u>0.871</u>	0.853	0.482	0.694	0.286	
	-	RF	<u>0.866</u>	0.837	<u>0.866</u>	0.847	0.470	0.681	1.029	
	-	LR	<u>0.881</u>	<u>0.872</u>	<u>0.881</u>	<u>0.870</u>	<u>0.536</u>	0.720	0.254	
	-	DT	0.835	0.843	0.835	0.838	0.465	0.702	0.338	
Custom CNN Models	1-Layer	FCGR	<u>0.863</u>	<u>0.831</u>	<u>0.863</u>	<u>0.844</u>	<u>0.490</u>	<u>0.677</u>	<u>0.357</u>	
		Spike2CGR	0.783	0.613	0.783	0.687	0.219	0.500	0.999	
		RandomCGR	0.792	0.638	0.792	0.707	0.221	0.497	0.404	
		Bézier	0.835	0.779	0.835	0.781	0.314	0.548	0.805	
	% improv. of Bézier from -2.8 -5.2 -2.8 -6.3 -17.6 -12.9 -125.49									
	FCGR									
	2-Layer	FCGR	0.852	0.833	0.852	0.837	0.489	0.676	0.419	
		Spike2CGR	0.783	0.613	0.783	0.687	0.219	0.500	1.196	
		RandomCGR	0.800	0.640	0.800	0.711	0.222	0.500	0.389	
		Bézier	0.814	0.795	0.814	0.803	0.419	0.633	0.626	
	% improv. of Bézier from -3.8 -3.8 -3.8 -3.4 -7 -4.3 -49.40									
	FCGR									
	3-Layer	FCGR	0.800	0.640	0.800	0.711	0.222	0.500	0.490	
		Spike2CGR	0.783	0.612	0.783	0.687	0.219	0.500	1.456	
		RandomCGR	0.800	0.640	0.800	0.711	0.222	0.500	0.391	
		Bézier	0.830	0.748	0.830	0.780	0.296	0.541	0.637	
% improv. of Bézier from 3 10.8 3 6.9 7.4 4.1 -30										
FCGR										
4-Layer	FCGR	0.831	0.735	0.831	0.779	0.329	0.586	0.498		
	Spike2CGR	0.783	0.612	0.783	0.687	0.219	0.500	1.776		
	RandomCGR	0.800	0.640	0.800	0.711	0.222	0.500	0.435		
	Bézier	0.825	0.681	0.825	0.746	0.226	0.500	0.668		
% improv. of Bézier from -0.6 -5.4 -0.6 -3.3 -10.3 -8.6 -34.13										
FCGR										
Vision Transformer	ViT	FCGR	0.767	0.588	0.767	0.666	0.217	0.500	0.031	
		Spike2CGR	0.754	0.487	0.74	0.565	0.211	0.500	0.650	
		RandomCGR	0.756	0.512	0.756	0.632	0.201	0.500	0.032	
		Bézier	0.825	0.681	0.825	0.746	0.226	0.500	0.027	
	% improv. of Bézier from 5.8 9.3 5.8 8 0.9 0 12.90									
FCGR										
ResNet-50	ResNet-50	FCGR	0.800	0.642	0.800	0.712	0.222	0.501	1.317	
		Spike2CGR	0.770	0.559	0.770	0.654	0.198	0.500	2.290	
		RandomCGR	0.800	0.640	0.800	0.711	0.222	0.500	1.387	
		Bézier	0.835	0.780	0.835	0.796	0.334	0.601	0.175	
	% improv. of Bézier from 3.5 13.8 3.5 8.4 11.2 10 86.71									
FCGR										
VGG-19	VGG-19	FCGR	0.803	0.684	0.803	0.720	0.243	0.509	1.189	
		Spike2CGR	0.765	0.650	0.765	0.650	0.200	0.500	2.111	
		RandomCGR	0.800	0.640	0.800	0.711	0.222	0.500	1.054	
		Bézier	0.825	0.681	0.825	0.746	0.226	0.500	2.144	
	% improv. of Bézier from 2.2 -0.3 2.2 2.6 -1.7 -0.9 -80.31									
FCGR										
DenseNet	DenseNet	FCGR	0.116	0.013	0.116	0.024	0.052	0.500	0.987	
		Spike2CGR	0.116	0.011	0.116	0.022	0.050	0.500	1.767	
		RandomCGR	0.095	0.011	0.095	0.010	0.095	0.500	1.381	
		Bézier	0.105	0.011	0.105	0.020	0.105	0.500	1.211	
	% improv. of Bézier from -1.1 -0.2 -1.1 -0.4 5.3 0 -22.69									
FCGR										
EfficientNet	EfficientNet	FCGR	0.089	0.008	0.089	0.014	0.041	0.500	1.622	
		Spike2CGR	0.085	0.005	0.085	0.009	0.008	0.500	2.221	
		RandomCGR	0.028	0.002	0.028	0.004	0.027	0.500	1.988	
		Bézier	0.058	0.003	0.058	0.006	0.027	0.500	1.566	
	% improv. of Bézier from -3.1 -0.5 -3.1 -0.8 -1.4 0 3.45									
FCGR										

Table 15: Classification results for different models and algorithms for ACPs (Breast Cancer) dataset. The top 5% values for each metric are underlined.

lapping. This is an implication that the embeddings created by both these methods are almost similar in quality as they possess somehow similar data preservation patterns in a low-dimensional space.

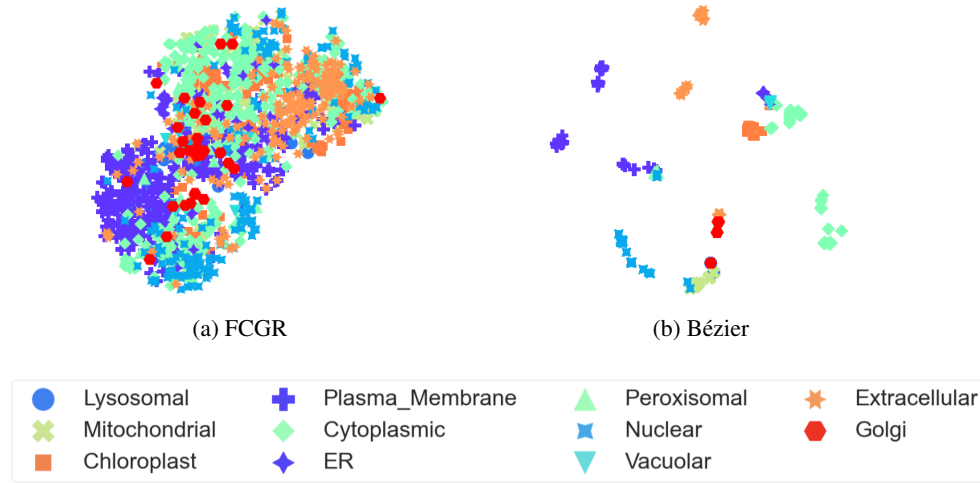


Fig. 11: The t-SNE plots of **Protein Subcellular Localization dataset** embeddings extracted from the last layer of **2layer CNN** classifier using the FCGR- and Bézier-based images, respectively. The figure is best seen in color.

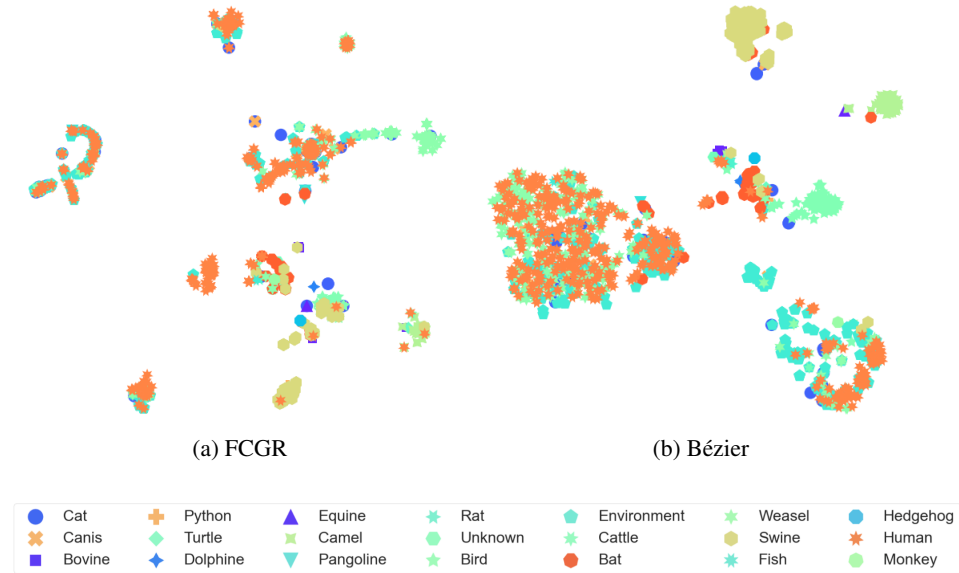


Fig. 12: The t-SNE plots of **Coronavirus Host dataset** embeddings extracted from the last layer of **2layer CNN** classifier using the FCGR- and Bézier-based images, respectively. The figure is best seen in color.

Furthermore, the t-SNE visualization of the ACP dataset is given in Figure 13. It also portrays a very similar cluster structure for both FCGR and Bézier methods. The clusters are very scattered, non-definite, and overlapping, which indicates that the respective embeddings are unable to preserve the data structure in 2D space.

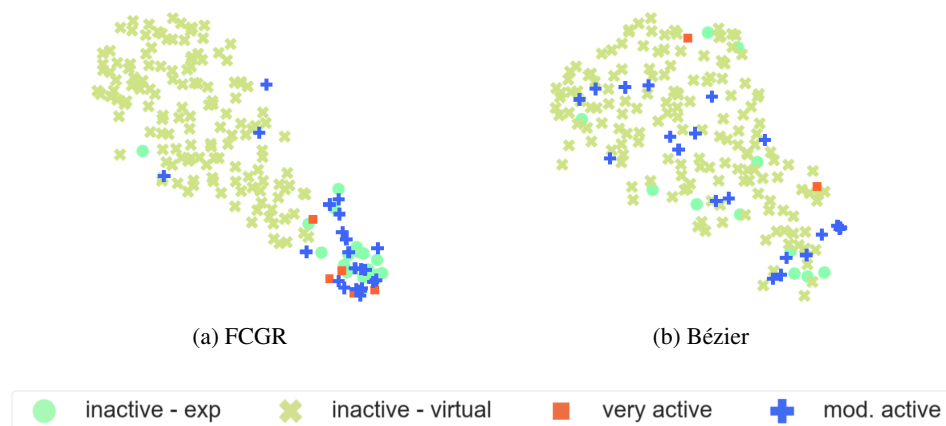


Fig. 13: The t-SNE plots of **ACP dataset** embeddings extracted from the last layer of **2layer CNN** classifier using the FCGR- and Bézier-based images respectively. The figure is best seen in color.

The t-SNE plots of the Human DNA dataset are given in Figure 14. We can observe that the Bézier-based clusters are more compact while FCGR ones are very scattered.

#### F.4 Inter-Class Correlation

To analyze the correlation between different classes of our respective datasets we utilized the heat maps. These maps are generated from the embeddings extracted from the last layer of the 2-layer CNN classifier corresponding to FCGR and Bézier based images respectively. To construct the maps, first pairwise cosine similarity scores are computed between embeddings of different classes and then an average value is calculated to get a score for a class. Note that the maps are normalized between [0-1] to the identity pattern.

The heat maps of the protein subcellular dataset corresponding to FCGR and our proposed method are demonstrated in Figure 15. We can observe that in the case of FCGR, although each class has a maximum correlation with itself, some of them also portray a high correlation with each other as well. For instance, the "Golgi" class shows a high similarity to "ER" and "Pero" etc. This indicates that distinguishing different classes is hard using the embeddings generated by FCGR, hence the FCGR images are suboptimal representations. However, the heat map constructed from the Bézier images shows that each class has maximum similarity to itself only and holds almost no correlation with other classes. It is an implication that the embeddings generated

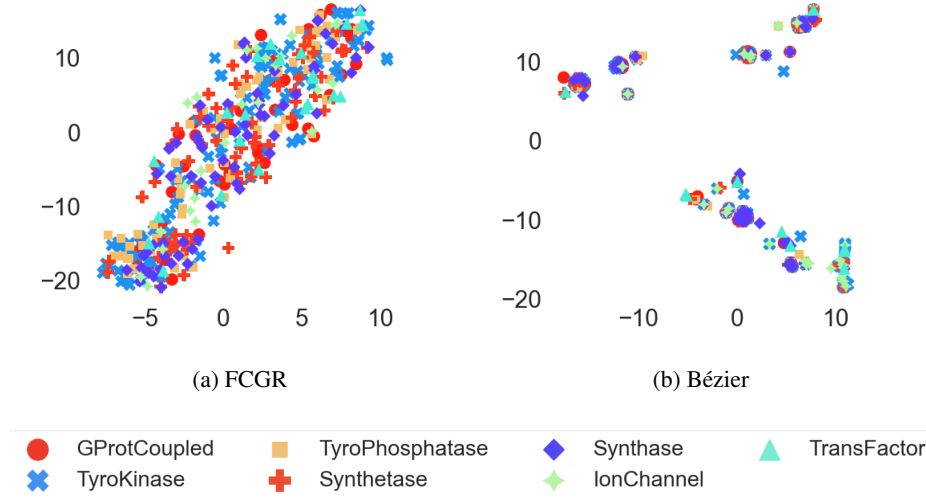


Fig. 14: The t-SNE plots of **Human dataset** embeddings extracted from the last layer of **2layer CNN** classifier using the FCGR- and Bézier-based images respectively. The figure is best seen in color.

from the Bézier method belonging to the same class are very similar to each other while highly distinct from the embeddings of other classes. Hence, the Bézier-based images are optimal, and this can also be proven by the classification performance they achieved for our respective dataset.

Similarly, the heat maps for cosine similarity of the Coronavirus host dataset corresponding to FCGR and Bézier encoding methods are shown in Figure 16. We can observe that for both methods, each class has maximum similarity to itself. However, some of the classes also portray a correlation with other classes, like "Weasel" is highly correlated to "cat" & "can" classes, etc. This means that although the embeddings generated by both FCGR and Bézier which belong to the same class are very similar to each other, they can also be similar to embeddings from some of the other classes.

Furthermore, the heat maps corresponding to the Human DNA dataset are given in Figure 17. We can observe that, in all the maps, each class shows maximum similarity to itself.

## F.5 Interpretability

To further evaluate the effectiveness of the created images by FCGR and Bézier methods, we plotted the histograms of the respective embeddings extracted from the last layer of the 2-layer CNN model against the protein subcellular dataset. We employ the 2-layer CNN model because it demonstrates good classification performance for both FCGR and Bézier methods.

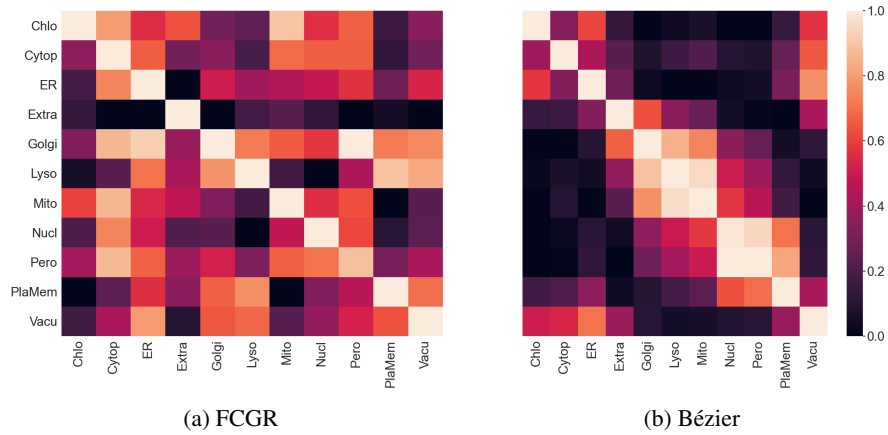


Fig. 15: Heatmap for cosine similarity between different **Protein Subcellular Localization** pairs for FCGR and Bézier-based image generation methods corresponding to 2layer CNN classifier.

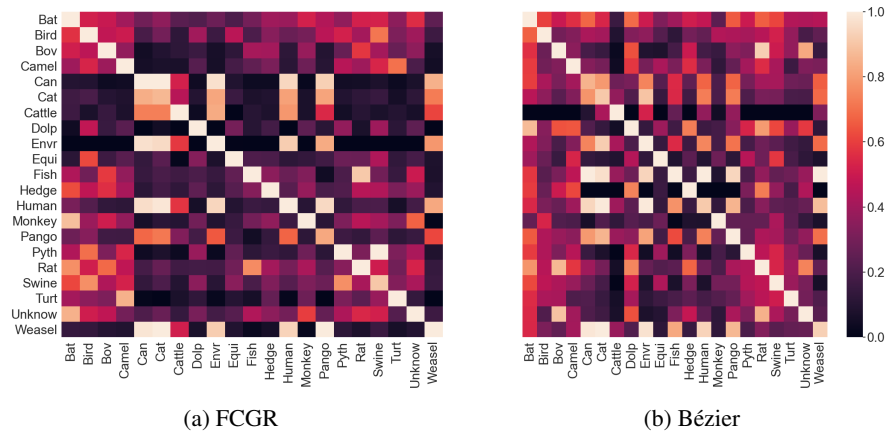


Fig. 16: Heatmap for cosine similarity between different **Coronavirus Host** pairs for FCGR and Bézier-based image generation methods corresponding to 2layer CNN classifier.

The Bézier images-based histograms of the protein subcellular dataset are shown in Figure 18. We can observe that, although the embeddings of (a) & (b) belong to the same label Lysosomal, they yield different histograms which indicate that the information in the respective images is captured differently for different sequences by our Bézier method. Moreover, as they belong to the same category, the Euclidean distance between

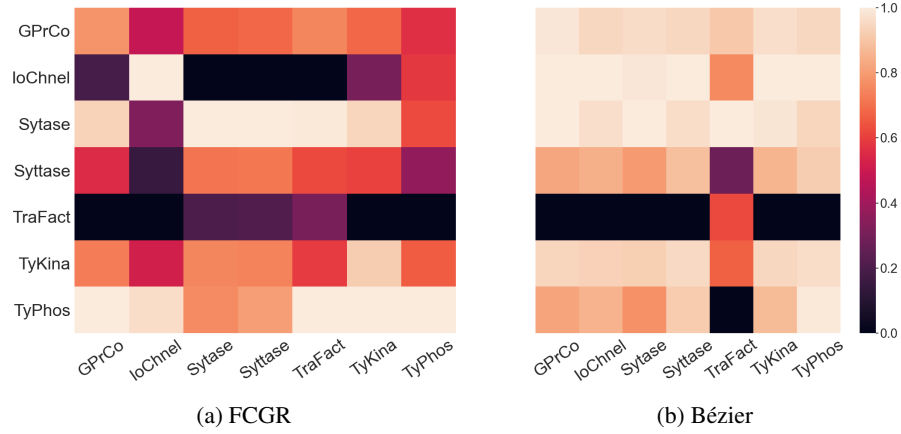


Fig. 17: Heatmap for cosine similarity between different **Human DNA** pairs for FCGR and Bézier-based image generation methods corresponding to 2layer CNN classifier.

them is small (0.17), while the distance for embeddings from different categories is large as shown in (c) & (d) which is 0.87. This implies that our method is effective as it keeps similar instances close to each other while the different ones are far from each other.

Similarly, the histograms for FCGR images-based embeddings are illustrated in Figure 19. We can see that the Euclidean distance between the embeddings from the same Lysosomal category ((a) & (b)) is very large (0.88) and it's not a desirable behavior. This indicates that the images generated by FCGR are suboptimal representations of the sequences.

## F.6 Confusion Matrix Results And Discussion

The confusion matrices for the host dataset are given in Figure 20. We can observe that although FCGR has a high number of true positive values for most of the classes, our method also portrays comparable results. Note that our technique has a high true positive count for the human class, which is the most frequent class in the dataset, as compared to the FCGR method.

Similarly, the confusion matrices for the Human DNA dataset are illustrated in Figure 21, and they portray similar patterns as the host dataset's matrices.

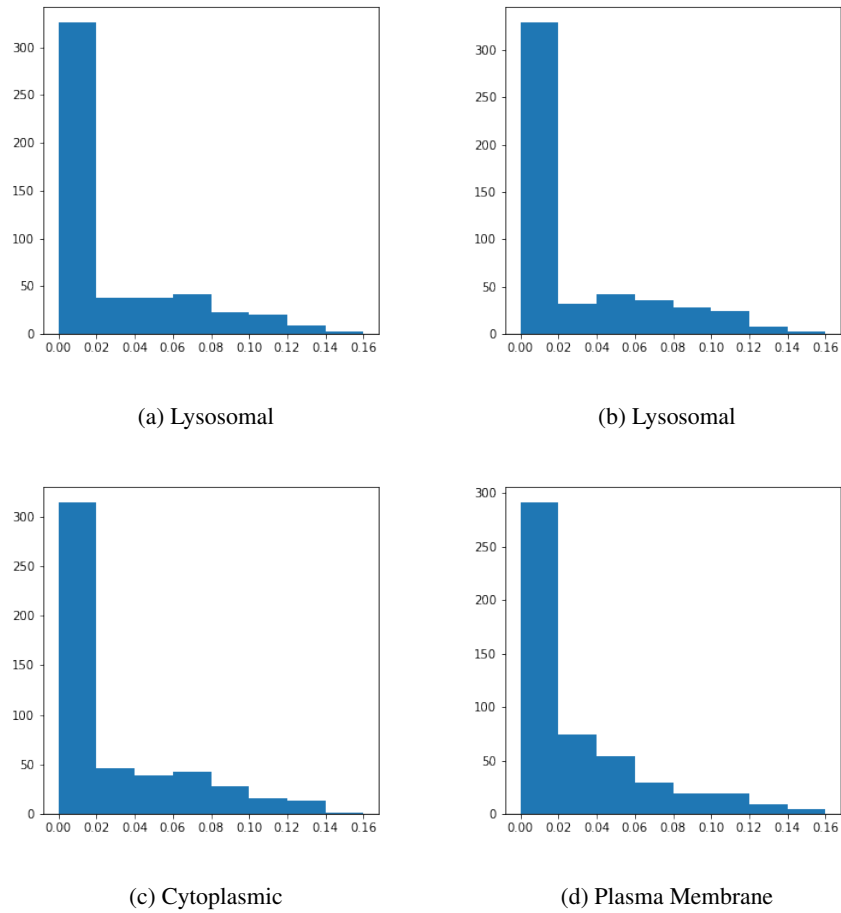


Fig. 18: The histogram of embeddings extracted from the last layer of the 2-layer CNN model for the **Bézier**-based images of **Protein Subcellular dataset**. (a) & (b) shows the plots for two different embeddings belonging to the **Lysosomal** class and they have a **0.17** Euclidean distance. (c) & (d) contain the histograms of embeddings belonging to **Cytoplasmic** and **Plasma Membrane** classes respectively, and they have an Euclidean distance of **0.87**.

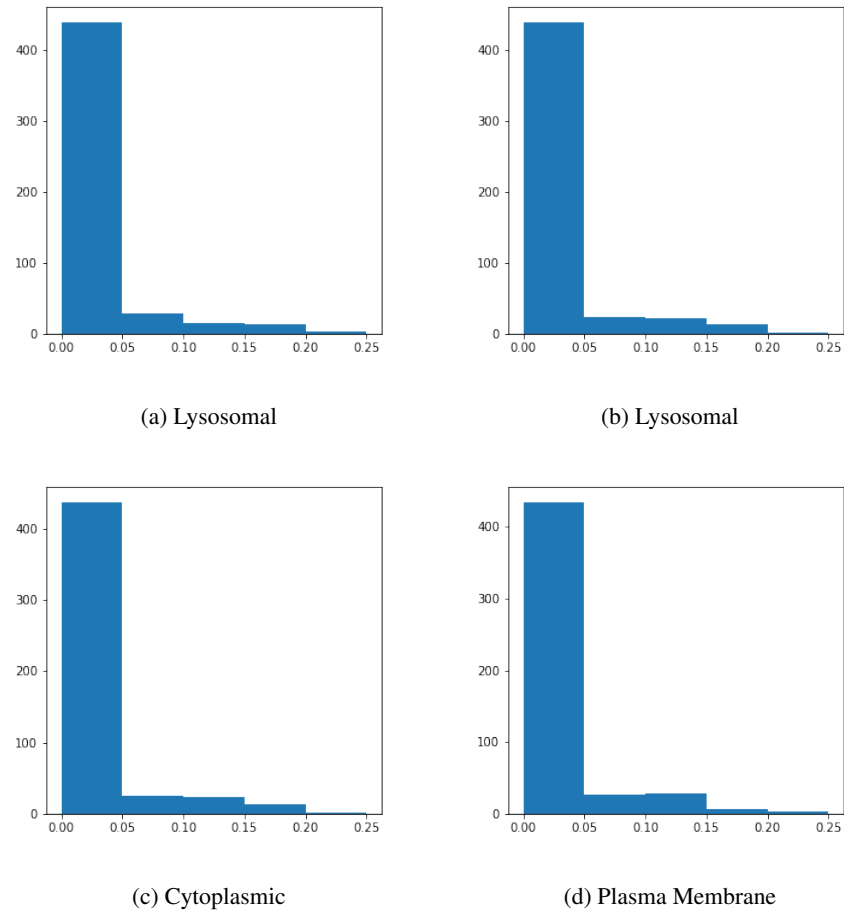


Fig. 19: The histogram of embeddings extracted from the last layer of the 2-layer CNN model for the **FCGR**-based images of **Protein Subcellular dataset**. (a) & (b) shows the plots for two different embeddings belonging to the **Lysosomal** class, and they have a **0.88** Euclidean distance. (c) & (d) contain the histograms of embeddings belonging to **Cytoplasmic** and **Plasma Membrane** classes respectively, and they have an Euclidean distance of **1.30**.

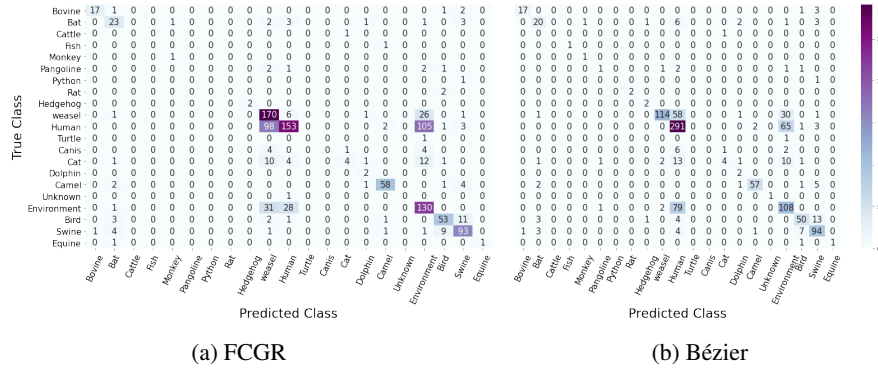


Fig. 20: Confusion matrices of **Coronavirus host dataset** for **2layer CNN classifier** using the FCGR- and Bézier-based image generation methods.

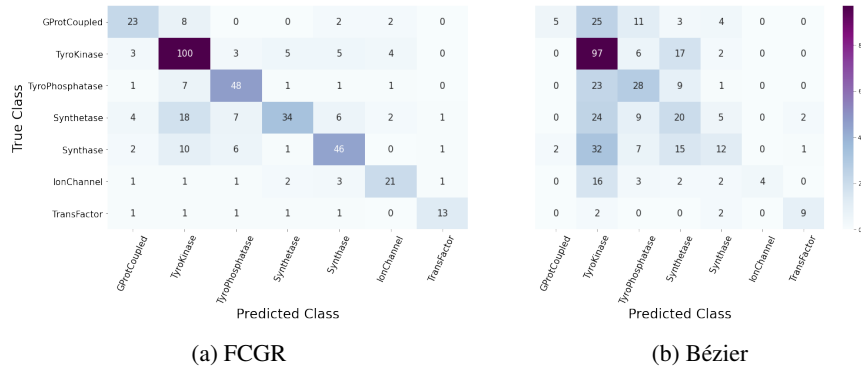


Fig. 21: Confusion matrices of **Human DNA dataset** for **2layer CNN classifier** using the FCGR- and Bézier-based image generation methods.